RSC Advances

PAPER

View Article Online
View Journal | View Issue

Cite this: *RSC Adv.*, 2025, **15**, 45196

Improved photocatalytic activity and enhanced germination rate of *Oryza sativa* and urea sensor development utilizing fabricated NiO·SrCO$_3$·ZnO nanomaterials

Shubrojit Dey,[a] Pallab Chandra Saha,[ab] Md Abdus Subhan,*[a] Md Mahmud Alam,[c] Mohammad Al-Mamun,[d] Didar Hossain,[e] Abul Kalam Azad,[e] Saeed D. Alahmari,[f] Abdulkarim Albishri,[g] Khalid A. Alzahrani[h] and Mohammed Muzibur Rahman*[h]

In this approach, novel NiO·SrCO$_3$·ZnO nanomaterials (NMs) were synthesized using a facile co-precipitation technique. The produced NMs were characterized using XRD, SEM, EDS, FTIR, PL, and Raman spectroscopy. The average particle size was 32.35 nm, as determined by XRD. The Raman spectrum of NiO·SrCO$_3$·ZnO exhibited characteristic peaks for NiO (509 cm^{-1}), SrCO$_3$ (147, 179, 242, 700, and 1071 cm^{-1}), and ZnO (101 and 359 cm^{-1}). The photocatalytic activity of the nanomaterial was assessed using methylene blue (MB) as a model dye under various conditions, including pH, temperature, and reusability in visible light. The highest efficiency was observed to be 98.41% for a 0.06 g L^{-1} dose of NM in a basic medium (pH 9.2). The growth of pathogenic bacteria, both Gram-positive and Gram-negative, was significantly reduced by the NMs. In this innovative strategy, ternary NiO·SrCO$_3$·ZnO NMs were utilized for promoting seed germination, which potentially enhanced the germination of *Oryza sativa* seeds. Therefore, the fabricated NiO·SrCO$_3$·ZnO NMs have significant promise for use in the development of effective photocatalytic systems and industrial sterilizing agents, and as good promoters of seed germination. This paper also focuses on developing a novel urea sensor employing NiO·SrCO$_3$·ZnO NMs coated on a glassy carbon electrode (GCE) with the help of 5% Nafion as a conducting chemical coating binder. The electrochemical performance of the fabricated electrode (NiO·SrCO$_3$·ZnO NMs/Nafion/GCE) was assessed *via I–V* techniques, revealing a remarkable sensitivity of 23.5189 μA μM^{-1} cm^{-2} and a linear dynamic range from 0.1 nM to 0.01 mM. The sensor exhibited a limit of detection of 4.31 ± 0.22 pM, underscoring its potential for highly sensitive urea detection amid various applications. These findings emphasize the effectiveness of NiO·SrCO$_3$·ZnO NMs in enhancing the electrochemical performance of urea sensors.

Received 25th August 2025
Accepted 24th October 2025

DOI: 10.1039/d5ra06318c

rsc.li/rsc-advances

Introduction

Owing to its unique physical and chemical properties, nano-multimetal oxide (NMMO) is utilized in various fields, including chemistry, physics, engineering, nanobiotechnology, and medicine. In addition to optical,[1] electrical,[2] magnetic,[3] and adsorbent capabilities,[4] they exhibit anomalous diffusion, supercapacitive characteristics, and porous behavior.[5] NMMOs have diverse applications, including photocatalytic,[6] solar cells,[7] fuel cells,[8] lithium-ion batteries,[9] light-emitting devices (LEDs),[10] sensors,[11] and photodetectors.[12] Furthermore, NMMOs have many biological applications, such as in drug delivery,[13] cancer therapy,[14] antibacterial[15] and antimicrobial[16] applications, and fluorescent imaging.[17]

NMMOs with a wide band gap can form semiconductor materials.[18] The optical, electrical, and thermal properties of

[a]*Department of Chemistry, School of Physical Sciences, Shahjalal University of Science and Technology, Sylhet-3114, Bangladesh. E-mail: subhan–che@sust.edu*
[b]*Department of Chemistry, University of Virginia, Charlottesville, VA, 22904, USA*
[c]*Department of Chemical Engineering, Z. H. Sikder University of Science and Technology (ZHSUST), Shariatpur-8024, Bangladesh*
[d]*Centre for Clean Environment and Energy, Griffith School of Environment, Gold Coast Campus, Griffith University, QLD 4222, Australia*
[e]*Department of Genetic Engineering & Biotechnology, Shahjalal University of Science and Technology, Sylhet-3114, Bangladesh*
[f]*Department of Physical Sciences, Chemistry Division, College of Science, Jazan University, P.O. Box 2097, 45142 Jazan, Saudi Arabia*
[g]*Department of Chemistry, College of Sciences & Arts, King Abdulaziz University, Rabigh, Kingdom of Saudi Arabia*
[h]*Center of Excellence for Advanced Materials Research (CEAMR), Chemistry Department, Faculty of Science, King Abdulaziz University, Saudi Arabia. E-mail: mmrahman@kau.sa.edu; Tel: +966596421830*

semiconductor metal oxides stand out as crucial features in devices for detecting and identifying potentially explosive and unsafe gases. Nickel oxide nanoparticles have a band gap that spans 3.6 to 4.0 eV. The band gap increases with the annealing temperature.[19] Both Gram-positive and Gram-negative bacteria respond to NiO NPs.[20] Due to its exceptional chemical stability and strong catalytic activity, it is a suitable photocatalyst material for environmentally friendly applications involving the breakdown of azo dyes.[21] The NiO NPs have a beneficial effect on the germination of radish and *Vigna radiata* seeds.[22,23]

In degrading MB dye, $SrCO_3$ has demonstrated its effectiveness as a photocatalytic agent, with 98.2% MB degraded after 180 minutes of exposure to visible light.[24] Its strong physicochemical qualities and broad bandgap (3.17 eV) allow its use as a capping agent.[25] $SrCO_3$ NPs can also be used as a nanocarrier for targeted therapy.[26]

ZnO NPs have important biochemical features that have significant applications in the agricultural industry. The germination of rice seeds can be significantly impacted by the optimum usage of ZnO NP. ZnO NP concentrations of 50 and 100 mg L^{-1} have favorable effects on *Oryza sativa* development. Furthermore, it might be useful for lowering the buildup of arsenic (As) during germination.[27,28]

Significant roles are played by reactive oxygen species (ROS) in the toxicity mechanisms of metal oxide NPs. ROS has a substantial role in photodegradation, bacterial killing, and germination. During the process of photocatalytic dye degradation, metal oxide NPs, such as ZnO, produce ROS, including $^{\bullet}O_2^-$ and $^{\bullet}OH$.[29–32] It has been revealed that several metal oxide NPs, including ZnO NPs, are effective against a variety of bacteria, including photobacteria, *Bacillus subtilis*, *Escherichia coli*, and *Streptococcus aureus*. ROS are frequently held accountable for the toxicity of metal oxide NPs.[33–35] Although ROS has historically been thought of as a plant-destructive agent, it has recently been shown that ROS aids in the germination of seeds. ROS can be produced from oxygen. H_2O_2 is also a significant ROS agent since it may easily cross different types of cell membranes. The seed becomes biologically active, germination-capable from the mother plant's quiescent seed by the creation of ROS inside the seed. Several metal oxide NPs, such as NiO and ZnO, play a vital role in plant growth through the ROS mechanism.[23,27,28,36,37]

Because of the various substantial applications of NiO, ZnO, and $SrCO_3$ NPs discussed above, we intended to construct a novel composite metal oxide $NiO \cdot SrCO_3 \cdot ZnO$ for multifunctional applications, as addressed in the present study. Using a facile coprecipitation approach, we created multimetal oxide-based $NiO \cdot SrCO_3 \cdot ZnO$ NMs in this study to examine their effectiveness in the photocatalysis of Methylene Blue (MB) dye degradation, antibacterial activities, and rice seed germination studies. The structural and morphological characteristics of the $NiO \cdot SrCO_3 \cdot ZnO$ NMs were investigated using several methods. Following the synthesis of $NiO \cdot SrCO_3 \cdot ZnO$ NMs, we assessed their catalytic activity and found that they performed better in a basic medium than in either acidic or neutral medium. Additionally, both Gram-positive and Gram-negative bacteria responded to the NM's antibacterial activity. Subsequently, we investigated the role of the $NiO \cdot SrCO_3 \cdot ZnO$ NMs in the growth of rice seeds, which also produced excellent results in laboratory studies.

As a versatile compound, urea has numerous industrial applications due to its nitrogen content, playing a significant role in sectors such as fertilizers, chemical feedstock, animal feed, pharmaceuticals, the textile industry, and resin production. This widespread use raises the risk of urea contamination in environmental water systems, underscoring the urgent need for effective detection and remediation methods to promote a sustainable environment.[38,39] Urea in blood is a crucial indicator for assessing kidney function and metabolic health, making its accurate detection vital for clinical diagnostics and environmental monitoring. Urea is a uremic toxin in patients with impaired kidneys. Thus, maintaining a suitable urea level in the blood is crucial for these patients, particularly patients with CKD (chronic kidney disease) and ESRD (end-stage renal disease).[40]

Traditional methods for measuring urea in various samples, mainly in clinical and environmental contexts, have been widely employed. Common techniques for urea detection include enzymatic assays,[41] colorimetric methods,[42] conductometric measurements,[43] high-performance liquid chromatography (HPLC),[44] spectrophotometry,[45] and titration.[46] While effective for both environmental monitoring and clinical diagnosis, these traditional methods often face challenges related to sensitivity, specificity, time efficiency, and equipment requirements. In response to these limitations, there is growing interest in alternative approaches, particularly electrochemical sensors.[47,48] These sensors offer rapid, sensitive, and cost-effective options for urea detection, effectively addressing the shortcomings of conventional techniques. By harnessing advancements in NMs and electrochemical methodologies, electrochemical sensors can significantly improve the accuracy and efficiency of urea measurement, enhancing health diagnostics and supporting environmental protection efforts.

Recent advancements in NMs have opened new avenues for enhancing the sensitivity and selectivity of electrochemical sensors. NiO, $SrCO_3$, and ZnO are promising candidates due to their unique electrical and electrochemical properties.[49–51] NiO exhibits excellent conductivity and electrocatalytic activity, while $SrCO_3$ contributes to enhanced stability and charge transfer.[52,53] ZnO, known for its high surface area and piezoelectric properties, can further improve sensor performance.[54,55] This paper proposes the development of a $NiO \cdot SrCO_3 \cdot ZnO$ nanomaterial-based electrochemical sensor for the efficient detection of urea. We intend to utilize the synergistic properties of these nanomaterials to develop a sensor that displays great sensitivity and selectivity while functioning under moderate conditions, rendering it appropriate for real-time applications. This introduction sets the stage for exploring the synthesis, characterization, and application of this innovative sensor, highlighting its potential impact on urea detection methodologies.

Experimental section

Materials

Nickel sulfate hexahydrate, $NiSO_4 \cdot 6H_2O$ (Smart-Lab, Indonesia), strontium chloride hexahydrate, $SrCl_2 \cdot 6H_2O$ (Sigma-

Aldrich), zinc sulfate heptahydrate, $ZnSO_4 \cdot 7H_2O$ (BDH Chemicals Ltd, Poole, England), and sodium carbonate, Na_2CO_3 (Smart-Lab, Indonesia) were used for synthesizing the NMs. For studying the photocatalytic activity, methylene blue (MB) $C_{16}H_{18}ClN_3S$ (Smart-Lab, Indonesia) dye was chosen. The hydroxyl radical was detected during photocatalysis by using sodium hydroxide, NaOH (Merck, Germany), and terephthalic acid, $C_8H_6O_4$ (Tokyo Chemical Industry Co., Ltd, >99.0%). Buffer capsules (pH 4, 7, and 9.2) (Smart-Lab, Indonesia) were used for the study of the pH effects on photocatalysis. For the germination study, 5.25% sodium hypochlorite, NaOCl, and for the detection of superoxide radical during the germination process, *p*-nitrotetrazolium blue (NBT) chloride, $C_{40}H_{30}Cl_2N_{10}O_6$ (Carl Roth GmbH and Co. KG, Schoemperlenstr. ≥98%), and tris(hydroxymethyl)aminomethane, $C_4H_{11}NO_3$ (BDH chemicals Ltd, Poole, England) were used.

Characterization techniques

X-ray diffraction (XRD, Bruker D8 Advance diffractometer, equipped with a graphite monochromator) was used to characterize the composition, bulk crystal phase, and other pertinent structural evidence of the materials examined in this work. Using the step scan approach, the diffraction patterns were recorded at 0.05 steps with a measurement rate of 10 s per step. The diffraction patterns were captured between 20° and 80° in the 2θ angle. Scanning electron microscopy (SEM, JEOL JSM-7100F) was used for the morphology observation. The elemental analysis was obtained with an X-ray energy dispersive spectrometer (EDS) (Oxford Instrument) equipped field-emission transmission electron microscope (HF-5000). Raman spectroscopy was carried out on a Renishaw inVia Raman Microscope with a 785 nm laser, 20× objective, and 100× objective. To guarantee that the exhibited spectra were typical, five measurements were taken for each sample. Peak fitting and background correction were performed using Renishaw Wire 5.0 software. A double beam UV-visible spectrophotometer (UV-1800 Series, UV-Vis spectrophotometer, Shimadzu Corporation, Kyoto, Japan), pH meter (model HI210 pH Meter, Hanna instruments, Romania), centrifuge (IEC SPINETTE centrifuge. DAMON/IEC Division), magnetic stirrer (Stuart Scientific), FTIR spectrophotometer (Shimadzu, IRPrestige-21), spectrofluorophotometer (Shimadzu Crop. Model RF-5301), electric muffle furnace (Gallenkamp, Korea), sonicator (GT SONIC–P2), and four-digit electronic balances (Shimadzu) were used in this work.

Preparation of $NiO \cdot SrCO_3 \cdot ZnO$ NMs

The $NiO \cdot SrCO_3 \cdot ZnO$ NMs were synthesized using a facile co-precipitation of carbonates from the aqueous solution of the metal salts. Initially, distilled water (DW) was used to prepare a solution (1.00 M, 50 mL) of Na_2CO_3 (5.995 g) and a solution (0.25 M, 50 mL) of $NiSO_4 \cdot 6H_2O$ (3.2804 g), $SrCl_2 \cdot 6H_2O$ (3.3325 g), and $ZnSO_4 \cdot 7H_2O$ (3.5917 g), respectively. After that, solutions of $NiSO_4 \cdot 6H_2O$, $SrCl_2 \cdot 6H_2O$, and $ZnSO_4 \cdot 7H_2O$ were combined in a beaker in a 1 : 1 : 1 ratio and rapidly agitated for five minutes at room temperature. The mixture was gradually mixed with agitation in a 1.00 M Na_2CO_3 solution until the carbonates of the metal salts completely precipitated out. The finished mixture was continuously swirled at 55–60 °C for 4 hours. The precipitate of metal carbonates was then filtered and repeatedly cleaned with DW. Following filtration, the precipitate was oven-dried for two hours at 120 °C. The dried precipitate was then heated to 400 °C, 600 °C, and 900 °C for five hours, respectively, in a muffle furnace to obtain the NMs. The process of calcination produced NMs. Due to the higher temperature needed for strontium oxide (>900 °C) formation, strontium carbonate was not decomposed into its oxide.[56]

The reaction of the NMs is as follows:

Precipitation steps,

$$(Ni^{2+} + SO^{4-}) + (2Na^{+} + CO_3^{2-}) \rightarrow NiCO_3 + (2Na^{+} + SO_4^{2-})$$

$$(Sr^{2+} + 2Cl^{-}) + (2Na^{+} + CO_3^{2-}) \rightarrow SrCO_3 + 2(Na^{+} + Cl^{-})$$

$$(Zn^{2+} + SO^{4-}) + (2Na^{+} + CO_3^{2-}) \rightarrow ZnCO_3 + (2Na^{+} + SO_4^{2-})$$

Calcination steps,

$$NiCO_3 \xrightarrow{\text{Calcination(400 °C, 600 °C, 900 °C)}} NiO + CO_2$$

$$SrCO_3 \xrightarrow{\text{Calcination(400 °C, 600 °C, 900 °C)}} SrCO_3$$

$$ZnCO_3 \xrightarrow{\text{Calcination(400 °C, 600 °C, 900 °C)}} ZnO + CO_2$$

$$NiO + SrCO_3 + ZnO \rightarrow NiO \cdot SrCO_3 \cdot ZnO$$

Hydroxyl radical ($^{\bullet}OH$) detection

The hydroxyl radical ($^{\bullet}OH$) of $NiO \cdot SrCO_3 \cdot ZnO$ NMs was detected by using terephthalic acid (TA) and sodium hydroxide. First, 8.6 mg of TA was taken in a beaker, then NaOH was added until all the TA reacted with NaOH in 100 mL of water. The solution was stirred for 1–2 hours due to the formation of sodium terephthalate salt.[57] To measure the quantity of $^{\bullet}OH$ produced from $NiO \cdot SrCO_3 \cdot ZnO$ NMs, TA was used as a probe molecule. Using different concentrations of NMs, $^{\bullet}OH$ radical generation was determined. First, a defined amount of NMs was added to the freshly prepared sodium terephthalate salt solution. Then the solution was stirred in a dark chamber for one hour. The solution was then irradiated under visible light (two 200 W, 220–240 volt tungsten filament light bulbs). TA reacts with $^{\bullet}OH$ to form 2-hydroxyterephthalic acid as a highly fluorescent product. After centrifugation, the quantity of 2-hydroxyterephthalic acid (which has a fluorescence peak at approximately 425 nm when excited with a wavelength of 315 nm light) was measured using a spectrofluorophotometer (Shimadzu Corp. Model RF-5301) to quantitatively examine the production of $^{\bullet}OH$.[58]

Preparation of priming solution

The seed priming test was conducted using the synthesized $NiO \cdot SrCO_3 \cdot ZnO$ NMs. By dispersing the NMs using a sonicator

(GT SONIC-P2) at 50 W and 40 kHz in DW for 20 minutes, 0.04 and 0.05 g L^{-1} amounts of NMs were designated as 40 and 50 ppm nano-priming agents, respectively. DW was used as a control.

Seed priming method and growth calculation

The germination study of *Oryza sativa*, which was approved by the Bangladesh Rice Research Institute (BRRI), was undertaken using $NiO \cdot SrCO_3 \cdot ZnO$ NMs. First, 100 seeds were washed and sterilized using 5.25% NaOCl (submerged for 10 min). Then, the seeds were washed with DW 2–3 times. For the seed priming technique, the surface-sterilized seeds were soaked in priming solutions (control, 40 ppm, and 50 ppm) for 24 h at room temperature.

After 24 hours of imbibition, the seeds were placed in a Petri dish containing filter paper. Each Petri dish contained 25 seeds. 5 mL of DW was added to the filter paper to wet the seeds. Then, the Petri dish was covered and placed in an incubator at room temperature. The germination of seeds was observed daily, and DW was added if necessary. After 7 days, the growth of the seeds (radicle and plumule lengths) was measured. The parameters of germination were measured by using the following equations:[59–61]

$$\text{Percent of germination (\%GP)} = \text{(total number of germinated seeds)/(total number of tested seeds)} \times 100$$

$$\text{Rate of germination (GR)} = (a/1) + (b - a/2) + (c - b/3) + \ldots + (n - n - 1/N)$$

where $a, b, c, \ldots, n$ are numbers of germinated seeds after 1, 2, 3, …, N days from the start of imbibition.

$$\text{Vigor index I} = \text{germination\%} \times \text{seedling length (cm)}$$

$$\text{Vigor index II} = \text{germination\%} \times \text{seedling dry weight (g)}$$

Histochemical localization of $^{\cdot}O_2^-$ during germination

In vivo identification of $^{\cdot}O_2^-$ formation was done using the NBT chloride staining agent. After 24 h of imbibition under the respective conditions (control, 40 ppm, and 50 ppm), 10 seeds were transferred to the Petri dish for incubation. After 2 days of incubation, the treated seeds were incubated for 1 h at room temperature in a solution of 1 mM NBT in 10 mM Tris–HCl (pH 7.0). The seeds were then washed twice with DW and photographed.[62]

Modification of GCE with co-doped $NiO \cdot SrCO_3 \cdot ZnO$ NMs

Fabrication of commercially obtained GCE with co-doped $NiO \cdot SrCO_3 \cdot ZnO$ NMs is crucial for developing a highly sensitive electrochemical sensor. To implement this change, a denser slurry of the co-doped $NiO \cdot SrCO_3 \cdot ZnO$ nanomaterials was created using ethanol and deposited as a thin coating over the glassy carbon electrode. The altered electrode was thereafter allowed to dry under standard laboratory conditions. To enhance the durability of the nanomaterial thin layer, several drops of Nafion adhesive were applied, and the electrode was then baked in an oven at 35 °C for one hour. The technique yielded a functional electrode consisting of co-doped $NiO \cdot SrCO_3 \cdot ZnO$ nanomaterials on the GCE. This electrode was then connected in series with a platinum wire to a Keithley electrometer, forming an electrochemical cell, or sensor. For urea detection, a 0.1 M urea stock solution was diluted with deionized water to provide a range of target solutions from 0.1 mM to 0.1 nM. A current–voltage analysis was performed with the constructed sensor, resulting in the development of a calibration curve that illustrated the relationship between current and urea content. The sensitivity of the area sensor was ascertained using the calibration curve, utilizing the slope and the surface area of the GCE (0.0316 cm^2). The longest linear segment of the curve permitted for estimating the linear detection range (LDR) for urea was determined, while the detection limit (DL) was defined based on a signal-to-noise ratio of 3. Equimolar quantities of mono- and disodium phosphate were combined to create the requisite buffer solutions. Throughout the study, a constant buffer volume of 10 mL was maintained in the sensing beaker during the *I–V* analysis of urea in the phosphate buffer phase.

Results and discussions

Characterization of $NiO \cdot SrCO_3 \cdot ZnO$ NMs

XRD analysis of $NiO \cdot SrCO_3 \cdot ZnO$ was carried out for structural characterization as well as to determine the phases and composition of the NMs, as depicted in Fig. 1(a). MDI Jade software was used to analyze the XRD data of the NMs. The produced NMs exhibit peaks at 2θ angles of 25.17° (1 1 1), 25.8° (0 2 1), 29.61° (0 0 2), 31.49° (0 1 2), 34.52° (1 0 2), 35.1° (2 0 0), 36.18° (1 1 2), 36.53° (1 3 0), 36.63° (0 2 2), 39.77° (2 1 1), 41.32° (2 2 0), 44.08° (2 2 1), 45.64° (0 4 1), 46.56° (2 0 2), 47.69° (1 3 2), 49.92° (1 1 3), 50.27° (0 2 3), 51.64° (2 2 2), 53.03° (0 4 2), 54.99° (3 1 0), 56.64° (2 4 0), 57.24° (3 1 1), 58.86° (2 4 1), 59.82° (1 5 1), 61.47° (0 0 4), 63.93° (3 3 0), 65.46° (1 1 4), 72.01° (3 3 2), 72.82° (2 0 4), and 73.73° (3 1 3). The pattern obtained for the $SrCO_3$ (matching PDF#74-1491, intensity matching 81%) indicated an orthorhombic structure with a space group of *Pnma*(62), cell dimensions (a) 6.02 Å, (b) 5.093 Å, (c) 8.376 Å, and angle (α) 90°. The unit cell volume of $SrCO_3$ is 256.8 $Å^3$. The corresponding peaks at 2θ values of 31.78° (1 0 0), 34.43° (0 0 2), 36.26° (1 0 1), 47.55° (1 0 2), 56.61° (1 1 0), 62.87° (1 0 3), 67.97° (1 1 2), 69.11° (2 0 1), 72.59° (0 0 4), and 76.99° (2 0 2) (matching PDF#89-0510, intensity matching 55%), suggest the presence of ZnO, which is hexagonal. The space group of ZnO is $P6_3mc$(186), with cell dimensions (a) 3.2488 Å, (b) 3.2488 Å, (c) 5.2054 Å, an angle (α) 90°, and a unit cell volume of 47.6 $Å^3$. Finally, the matching peaks of NiO at 2θ values of 37.23° (1 1 1), 43.25° (2 0 0), 62.83° (2 2 0), 75.35° (3 1 1), and 79.34° (2 2 2) (matching PDF#73-1523, intensity matching 36%) demonstrated the structure of NiO is cubic with $Fm\bar{3}m$(225) space group; cell dimensions (a) 4.188 Å, (b) 4.188 Å, (c) 4.188 Å and angle (α) 90°, and a unit cell volume of 73 $Å^3$. The XRD data were used to calculate the particle size, which was found to be 32.35 nm using Scherrer's formula, $\tau = K\lambda/(\beta \cos\theta)$. Where τ is the mean size, β is the line

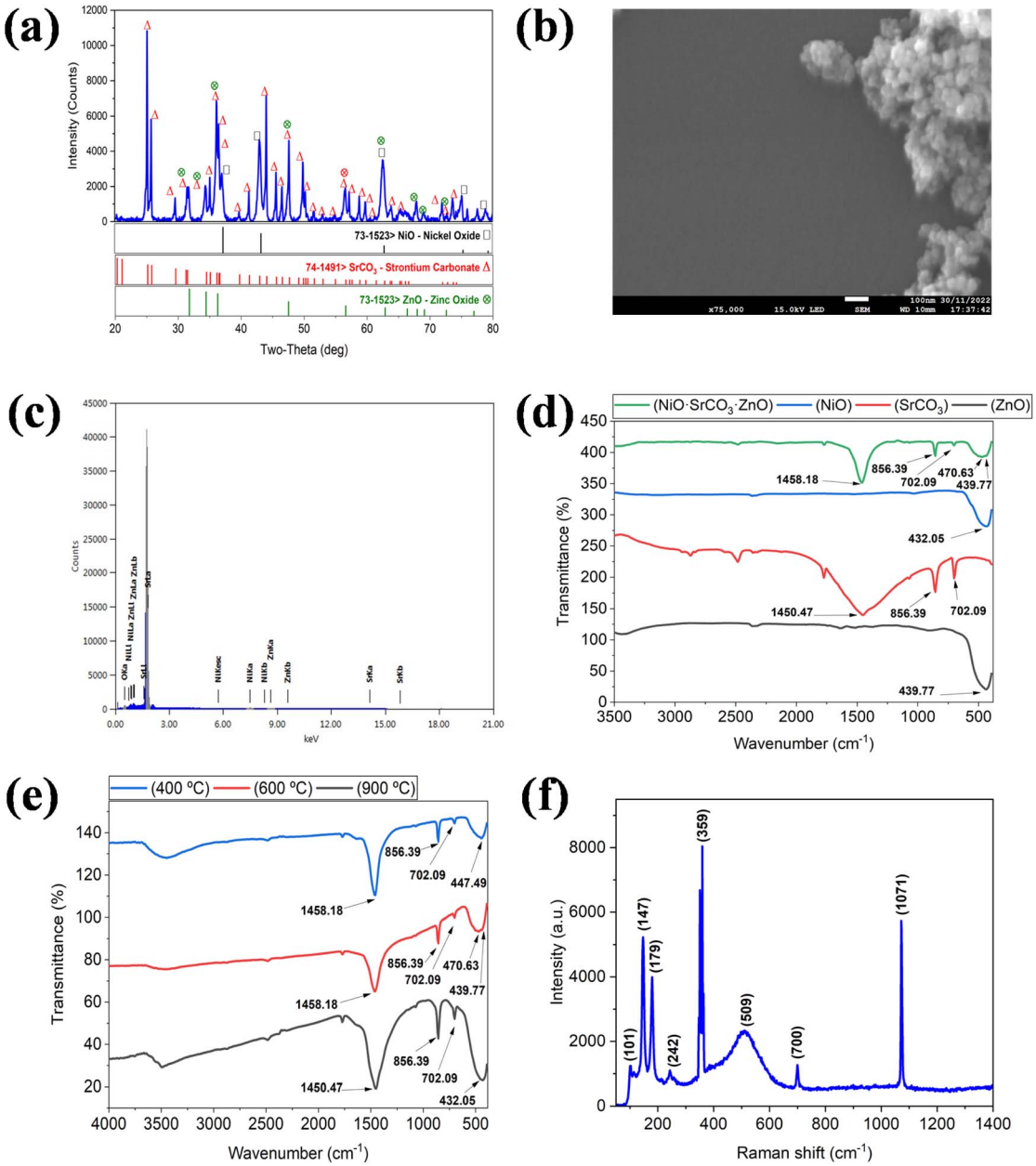

Fig. 1 (a) XRD spectrum, (b) SEM image, (c) EDS spectrum, FTIR spectrum with (d) single metal oxide and (e) at different calcined temperatures, and (f) Raman spectrum of the $NiO \cdot SrCO_3 \cdot ZnO$ NMs.

broadening at half the maximum intensity (FWHM), θ is the Bragg angle, and λ is the X-ray wavelength (0.1506 nm). K is a dimensionless form factor with a value of 0.94.

The phase percentage of NMs was calculated using the Reference Intensity Ratio (RIR) method. MDI Jade 6.5 was used for the quantitative analysis of XRD patterns using the following equation,

$$W_i = \frac{\frac{I_i}{RIR_i}}{\sum_{j=1}^{n} \frac{I_j}{RIR_j}} \times 100$$

where W_i is the weight fraction (weight percent, wt%) of phase i, I_i is the integrated intensity (area) of a main peak of phase i, and RIR_i is the corresponding RIR value.[63] The I_i and RIR_i values of the components are listed in Table S1. The calculated weight percentages of NiO, $SrCO_3$, and ZnO in $NiO \cdot SrCO_3 \cdot ZnO$ NMs were 15.97%, 58.50%, and 25.53%, respectively.

The scanning electron microscopy (SEM) images in Fig. 1(b) and S1 reveal the morphology of ternary $NiO \cdot SrCO_3 \cdot ZnO$ NMs at different magnifications, showing the existence of different phases. As demonstrated in the SEM images, the formation of a porous structure of nanoparticles was observed, which may have a high surface activity and good catalytic activity. The EDS spectrum of the $NiO \cdot SrCO_3 \cdot ZnO$ NMs is shown in Fig. 1(c). By using the EDS spectrum, the presence of four elements (Ni, Sr, Zn, and O) was determined. Furthermore, EDS mapping

(Fig. S2) demonstrated that the elements were not confined to a specific region but were instead distributed across the matrix.

The absorption spectra of $NiO{\cdot}SrCO_3{\cdot}ZnO$ NMs calcined at different temperatures were investigated by dispersing the NMs in acetone; the UV-Visible spectra are shown in Fig. S3. Two peaks were observed at 323 and 324 nm for 600 °C calcined samples. Additionally, only one peak at 324 nm for the 400 °C calcined sample, and a 323.7 nm peak for the 900 °C calcined sample was found. Analysis of the UV-visible spectra revealed the electronic energy levels of the composites.

Fig. 1(d) illustrates the FTIR spectrum of $NiO{\cdot}SrCO_3{\cdot}ZnO$ NMs. The bands of M–O and O–M–O vibration modes (M = Ni, Sr, Zn) appear in the 400–1000 cm^{-1} low-wavenumber region. FTIR spectra revealed the nature of the NiO NPs calcined at 600 °C. The Ni–O vibration was assigned to the band at 432.05 cm^{-1}.[64] For Zn–O, the frequency was assigned at 439.77 cm^{-1}.[65] In general, CO_3^{2-} exhibited D_{3h} symmetry and showed absorption bands between 400 and 1800 cm^{-1}. The strong absorption bands for $SrCO_3$ are centered at around 1450.47 cm^{-1} (in single $SrCO_3$) and 1458.18 cm^{-1} in $NiO{\cdot}SrCO_3{\cdot}ZnO$ NMs, and they are linked to the asymmetric stretching vibrations. Strong, narrow absorption bands for $SrCO_3$ are attributed to in-plane and out-of-plane bending vibrations at roughly 856.39 cm^{-1} and 702.09 cm^{-1}, respectively.[66] Fig. 1(e) shows the different calcination-temperature-dependent FTIR spectra. Here, we noticed that for 400 °C, 600 °C, and 900 °C temperatures, the $SrCO_3$ peaks were the same (702.09 and 856.39 cm^{-1}). However, for 400 °C and 900 °C, only one peak was noted for Ni–O and Zn–O (447.49 and 432.05 cm^{-1}, respectively).

The Raman spectrum of $NiO{\cdot}SrCO_3{\cdot}ZnO$ NMs is shown in Fig. 1(f); due to 1TO + 1 M (one-magnon), the mode was excited in Ni–O, with the peak at 509 cm^{-1}.[67] For $SrCO_3$, the peaks were observed at 147, 179, 242, 700, and 1071 cm^{-1}. Raman lines at 147 and 179 cm^{-1} were assigned to the angular oscillations of the A_{1g} and B_{2g} modes, respectively. The peaks at 242 cm^{-1} resulted from the carbonate group. The carbonate group (CO_3^{2-}) symmetric stretching mode ($_{v1}$–CO_3^{2-}) is responsible for the peak at 1071 cm^{-1}. The carbonate group A_{1g} –O–C–O in-plane bending is responsible for the symmetric bending mode of the low-intensity Raman mode observed at 700 cm^{-1}.[25,68] The two peaks of ZnO, 101 and 359 cm^{-1}, are assigned to the low-frequency E_2 mode and A_1(TO) mode, respectively.[69] Structural disorder, imperfections (such as a lack of oxygen or surface contaminants), and phonon confinement may all be contributing factors to this change in the Raman spectrum.

PL study of $NiO{\cdot}SrCO_3{\cdot}ZnO$ NMs

PL of the $NiO{\cdot}SrCO_3{\cdot}ZnO$ NMs was investigated in an acetone solution. Fig. 2 and Table S2 show the PL spectra of $NiO{\cdot}SrCO_3{\cdot}ZnO$ NM and compare them with single metal oxides and different calcination temperatures. Fig. 2(a–d) demonstrates the PL spectra of NMs (calcined at 600 °C), compared with NiO, $SrCO_3$, and ZnO, respectively. For the synthesized NMs, two emission peaks were noted at 382 and 466 nm wavelengths when

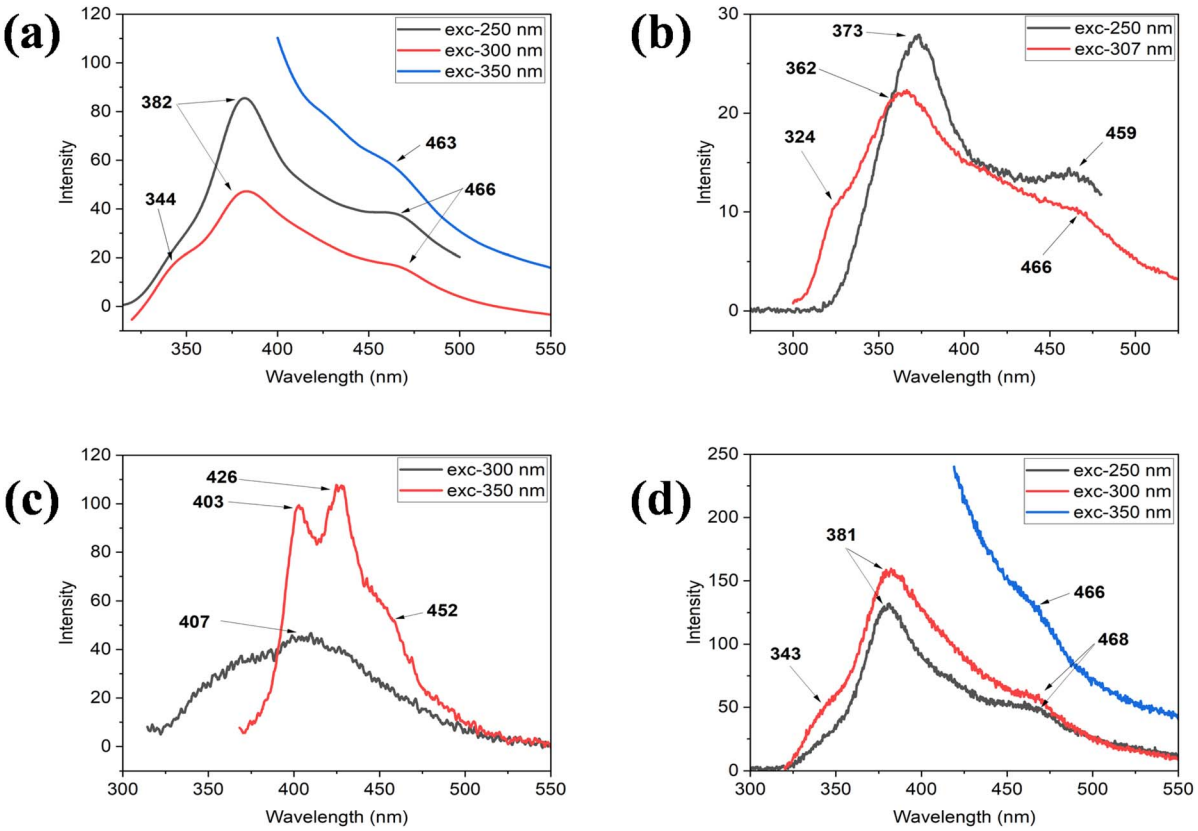

Fig. 2 PL spectra of (a) $NiO{\cdot}SrCO_3{\cdot}ZnO$ NMs, (b) NiO, (c) $SrCO_3$, and (d) ZnO at a calcination temperature of 600 °C.

the excitation was 250 nm. At 300 nm excitation wavelength, three peaks were observed (344, 382, and 466 nm). When the excitation was 350 nm, only one peak was noticed at 463 nm. For NiO, two peaks were noted at 373 and 459 nm for a 250 nm excitation wavelength. At 307 nm excitation, 3 peaks were observed (324, 362, and 466 nm). The near-band emission (NBE) of NiO is represented by a small peak at 324 nm. The recombination of excited electrons with holes in the valence band *via* radiative recombination is confirmed by the UV emission peaks at 362 and 373 nm. Two weak peaks in the emission spectra at 459 and 466 nm are caused by electron transport, which is facilitated by bandgap defects, such as oxygen vacancies.[70] For $SrCO_3$, the peaks were noted above 400 nm. At a 300 nm excitation wavelength, only one peak was observed at 407 nm. However, for 350 nm excitation, 3 peaks were seen (403, 426, and 452 nm). All the emission peaks of $SrCO_3$ were observed in the visible area known as deep-level emission (DPE) due to the structural defects in the crystal.[68] Also, for ZnO, two peaks were observed at 250 nm excitation wavelengths (381 and 468 nm). At 300 nm excitation, three peaks were exhibited (343, 381, and 468 nm). When the excitation was at 350 nm, a peak was observed at 466 nm. The excitonic transition from isolated regions below the transition band to the bottom of the valence band is responsible for the emission peaks at 343 and 381 nm, which are attributed to NBE. Additionally, recombination of the zinc interstitial (Zn_i) energy level and zinc vacancy (V_{Zn}) led to the observation of blue emission peaks at 470 and 492 nm.[71]

Fig. 2(a), S4, and Table S3 illustrate the different calcination-temperature-dependent PL spectra of $NiO \cdot SrCO_3 \cdot ZnO$ NMs. In both 400 °C and 600 °C calcined samples, similar emission spectra were observed. However, for the 900 °C calcined sample, different emission spectra were observed. Compared to 400 °C and 600 °C calcined samples, at 300 nm excitation wavelength, 2 peaks were exhibited (363 and 468 nm) for the 900 °C calcined sample. Additionally, at 350 nm excitation, a broad peak was detected at 406 nm. For a 346 nm excitation wavelength, 2 peaks were observed at 407 and 426 nm wavelengths.

Evaluation of photocatalytic activity

MB dye was used to test the photocatalytic performance of $NiO \cdot SrCO_3 \cdot ZnO$ NMs under ambient conditions. A varying volume of catalyst was added to the dye solution (100 mL, starting concentration 5.0 ppm), which was maintained in a cylindrical Pyrex beaker with a diameter of 5 cm. Before the irradiation, the solution was shaken for approximately one hour in the dark to ensure adsorption/desorption equilibrium. The visible light source was two 200 W, 220–240 volt tungsten filament light bulbs. The experimental dye solution and light source were placed 25 cm apart. Periodically, 4 mL of the solutions were collected, and, before analysis, dye solutions were separated from the photocatalyst by centrifugation. A Shimadzu-1800 double-beam spectrophotometer was used to quantify the change in dye solution concentration spectrophotometrically. Numerous catalyst doses were examined. The following equation was used to determine the catalytic efficiency of the dye degradation.

$$\text{Efficiency}(\%) = \frac{(C_0 - C_t)}{C_0} \times 100 = \frac{(A_0 - A_t)}{A_0} \times 100$$

where C_t and A_t represent the dye solution concentration and absorbance following radiation, respectively, and C_0 and A_0 represent the dye solution concentration and absorbance before radiation, respectively.

The effective dose of $NiO \cdot SrCO_3 \cdot ZnO$ NMs photocatalyst for dye removal when subjected to visible light irradiation was determined using a variety of doses, as shown in Fig. 3(a) and S5(a–e). Photocatalyst doses ranging from 0.04 g L^{-1} to 0.08 g L^{-1} were tested. The highest percentage of MB removal was at 0.06 g L^{-1}, with values for the individual concentrations of 0.04 g L^{-1}, 0.05 g L^{-1}, 0.06 g L^{-1}, 0.07 g L^{-1}, and 0.08 g L^{-1} being 97.33%, 97.86%, 98.41%, 97.87%, and 97.46%, respectively. As the quantity of photocatalyst was increased, the percentage of MB removal increased continuously up to 0.06 g L^{-1}, and then started to decrease.

The gradual removal of dye in the presence of $NiO \cdot SrCO_3 \cdot ZnO$ NMs photocatalyst at pH 9.2, 7, and 4 is shown in Fig. 3(b–d). After 240 minutes of visible light irradiation, the dye degradation efficiencies were found to be 98.41%, 92.99%, and 12.48% at pH 9.2, 7, and 4, respectively. At pH 9.2, $NiO \cdot SrCO_3 \cdot ZnO$ NMs generate hydroxyl radicals that enhance dye degradation; hence, the percentage of dye removal was determined to be outstanding in a basic medium (pH 9.2), moderate in a neutral medium (pH 7), and low in an acidic medium (pH 4). Dye degradation utilizing a metal oxide-based photocatalyst has been promising. According to Negash *et al.*,[72] the synthesised rGO@ZnO nanocomposites (NCs) showed superior MB dye degrading activity under solar radiation compared to bare rGO and ZnO. Higher performance was demonstrated by the catalyst at pH 8 (66%, 96.5%, and 99% for rGO, ZnO, and NCs after 100 min irradiation). Under UV light, NiO/ZnO NCs demonstrated MB dye degradation (94.02%, in 60 min).[73] ZnO–$SrCO_3$ NCs demonstrated the ability to remove MB dye under both visible and ultraviolet light, with better performance under UV light. After 120 minutes, 87.5% of the dye was eliminated under visible light, and 93.2% of the dye was eliminated under UV light.[74] Our study demonstrated that novel $NiO \cdot SrCO_3 \cdot ZnO$ NMs at pH 9.2 performed better as a photocatalyst under visible light irradiation, which has an impact on degrading industrial effluence under natural sunlight.

The plot of $\ln([MB]_0/[MB])$ *vs.* time shows a straight line with slope k for various pH values (Fig. 3(e)). The pseudo-first-order assumption provided a good description of the experimental results. The determined dye degradation rate constants (k) and the r-squared (r^2) values are listed in Table S4. For pH 4, 7, and 9.2, the r^2 values were 0.666, 0.9301, and 0.9316, respectively.

The photocatalytic activity of MB dye (5 ppm) was observed by using different calcined $NiO \cdot SrCO_3 \cdot ZnO$ NMs (400 °C, 600 °C, and 900 °C). $NiO \cdot SrCO_3 \cdot ZnO$ NMs calcined at 600 °C exhibited higher activity than the others (Fig. 3(f–h) and S5(f–h)).

In $NiO \cdot SrCO_3 \cdot ZnO$ NMs, the electrons in the valence bands (VB) could be stimulated to the conduction bands (CB) when the NMs are exposed to visible light with a photon energy greater than or equal to the NiO, $SrCO_3$, and ZnO band gaps. Upon the

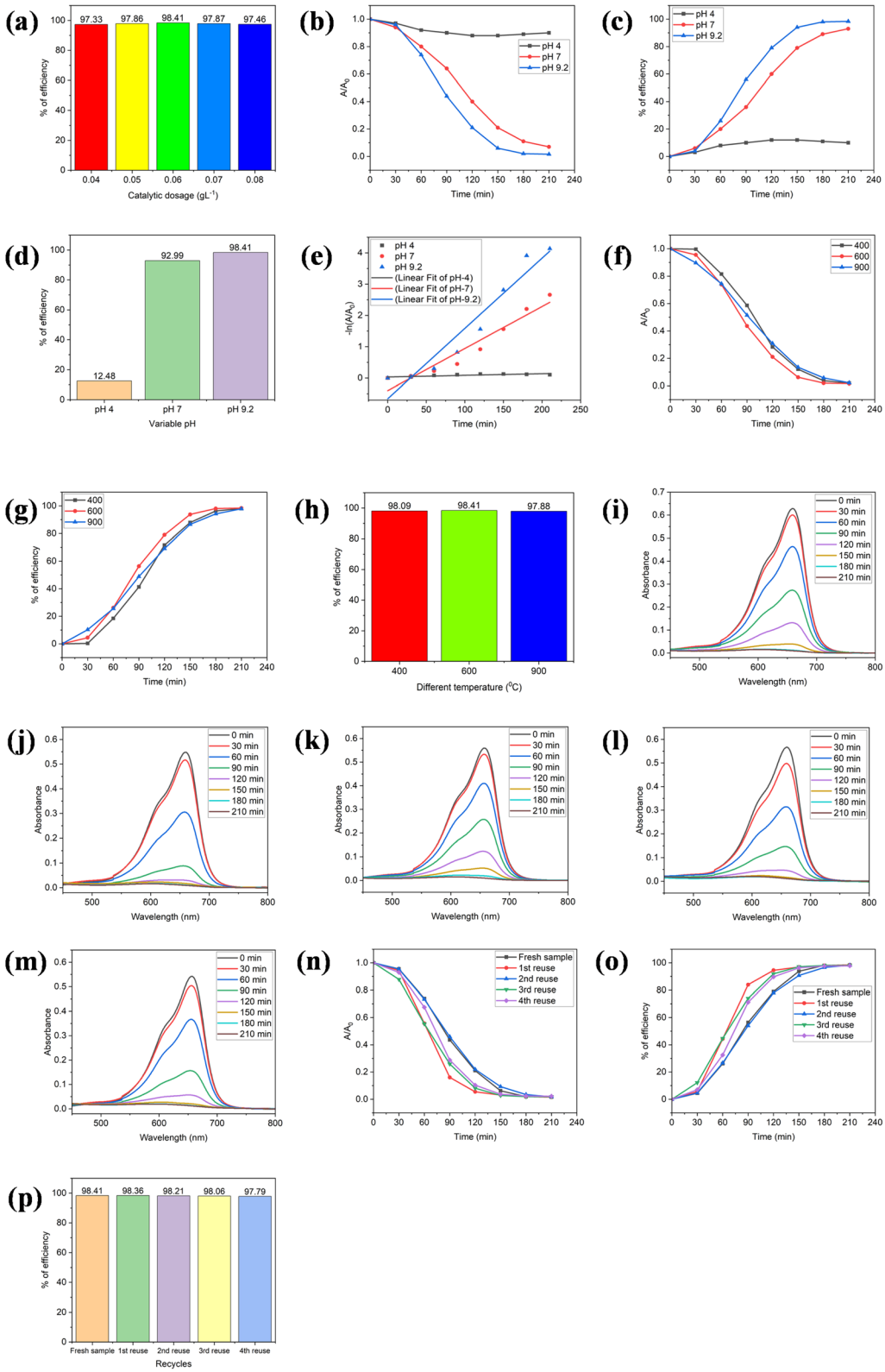

Fig. 3 Photocatalytic activity of the NiO·$SrCO_3$·ZnO NMs using MB dye (5 ppm) under visible light irradiation for 240 minutes, (a) dose effect, (b–d) pH effect, (e) kinetics study, (f–h) effect of different calcination temperatures, and (i–p) catalytic stability.

formation of a semiconductor heterostructure, a complementary energy band would form.[75] At the same time, the same number of holes could be generated in the VB. Electrical conduction in n-type semiconductors is mostly caused by electrons close to the conduction band minimum (CBM). This energy distortion, known as the n-type Schottky Barrier Height

(SBH), appears as a potential energy barrier that causes fixing behavior between the metal and the n-type semiconductor for electronic transport across the metal–semiconductor (MS) interface.[76,77] In $NiO \cdot SrCO_3 \cdot ZnO$, NiO is a p-type semiconductor while $SrCO_3$ and ZnO are n-type semiconductors. For p-type semiconductors, the Schottky barrier and charge spatial distribution are the key parameters of electron–hole separation and charge accumulation at the surface.[78] The degradation of MB dye is caused by the production of ROS ($^{\bullet}O_2^-$ and $^{\bullet}OH$) during energy transfer from the VB to the CB. The $^{\bullet}OH$ radicals that are generated are potent oxidizers. To scavenge the photogenerated electrons during the photocatalytic reaction, the catalyst produces ROS. The $^{\bullet}O_2^-$ radical is produced when electrons in the CB are swiftly captured by molecular oxygen adsorbed on the surface of the NMs and subsequently reduced. The proposed photocatalytic mechanism for MB dye degradation by experiment is as follows:

$$NiO \cdot SrCO_3 \cdot ZnO + h\nu \rightarrow h_{VB}^+ + e_{CB}^-$$

$$e_{CB}^- + h_{VB}^+ \rightarrow \rightarrow \text{energy}$$

$$h_{VB}^+ + H_2O \rightarrow H^+ + {}^{\bullet}OH$$

$$e_{CB}^- + O_2 \rightarrow {}^{\bullet}O_2^-$$

$$^{\bullet}OH + MB \rightarrow \text{intermediate products} \rightarrow H_2O + CO_2$$

$$^{\bullet}O_2^- + MB \rightarrow \text{intermediate products} \rightarrow H_2O + cCO_2$$

$$MB + e_{CB}^- \rightarrow \text{reduction products}$$

$$MB + h_{VB}^+ \rightarrow \text{oxidation products}$$

Stability of $NiO \cdot SrCO_3 \cdot ZnO$ nanomaterials as a photocatalyst

Recovery and reuse are key to the photocatalytic process because they reduce the cost of the system for treating wastewater and other processes. Using a catalyst only once is not economical or environmentally beneficial. The operational cost of the process, a crucial factor in the suitability of photocatalysts for wastewater purification, can be considerably reduced by an appropriately stable catalyst. In the Bangladesh textile industries, the real pH of the effluent is on average 8–11 due to the use of NaOH for material washing.[79] We believe the photocatalyst $NiO \cdot SrCO_3 \cdot ZnO$ can be used to remediate industrial effluent. As illustrated in Fig. 3(i–p), a catalytic stability assessment was conducted at pH 9.2 to determine whether the catalyst could be reused without experiencing a significant decline in performance. The process of regenerating the catalyst was simple. Following the completion of the initial photocatalytic dye degradation reaction, the solution was allowed to stand for 24 hours before the supernatant was separated. After that, distilled water and acetone were used to properly rinse the catalyst multiple times. The catalyst was then dried for 2 hours at 120 °C. Using MB dye solution, a series of tests were conducted using 0.06 g per L catalyst under visible light at pH 9.2 in order to assess the photocatalytic efficacy of the recycled catalyst. After the photocatalyst samples were separated and dried, the catalyst was utilized again for the degradation of a new MB solution under the same circumstances for every new cycle. After 3.5 hours of exposure to visible light, the MB solution's degradation percentages for 5 cycles were 98.41%, 98.36%, 98.21%, 98.06%, and 97.79%, respectively, in the presence of the $NiO \cdot SrCO_3 \cdot ZnO$ catalyst at pH 9.2. The adsorption of intermediate products on the photocatalyst's active sites, which prevents them from degrading new dye solutions, could be the cause of the decline in the degradation percentage. The catalyst's partial loss during separation could be another factor. Nevertheless, following the fourth photocatalyst reuse, 97.79% of MB was successfully degraded, meaning that the overall efficiency drop over the five cycles was only 0.62%. This suggests that the catalyst can be used to effectively remove the dye.

Hydroxyl radical ($^{\bullet}OH$) generation during photocatalysis

The $^{\bullet}OH$ radicals generated from $NiO \cdot SrCO_3 \cdot ZnO$ and the formation of sodium 2-hydroxyterephthalate by the reaction with sodium terephthalate were studied. Here, the reactant, sodium terephthalate, was not fluorescently active; however, the product, sodium 2-hydroxyterephthalate, was fluorescently active. The generation of $^{\bullet}OH$ radicals during photocatalysis of $NiO \cdot SrCO_3 \cdot ZnO$ NMs at different pH is shown in Fig. 4(a–d). Here, we observed that radical generation by the synthesized NMs was higher in the basic medium (pH 9.2) than in neutral (pH 7) or acidic media (pH 4). The results indicate that the synthesized $NiO \cdot SrCO_3 \cdot ZnO$ NMs can be a good catalyst for dye removal in a basic medium due to $^{\bullet}OH$ radical production. This was confirmed by the increase in photocatalytic degradation activity with $^{\bullet}OH$ radical generation (Fig. 3(b–d)).

Fig. 4(e–h) illustrates the production of $^{\bullet}OH$ radicals during the photocatalysis of $NiO \cdot SrCO_3 \cdot ZnO$ NMs calcined at different temperatures. Among 400 °C, 600 °C, and 900 °C calcination temperatures, NMs calcined at 600 °C generated the highest amount of radicals. 400 °C calcined NMs were the second-highest radical generator. The generation of $^{\bullet}OH$ radical by samples obtained at different calcination temperatures was harmonized with the MB dye removal (Fig. 3(f–h)).

Finally, the photocatalytic activity of $NiO \cdot SrCO_3 \cdot ZnO$ NMs demonstrated excellent performance through the degradation of the model dye, MB, driven by visible light and ROS. $NiO \cdot SrCO_3 \cdot ZnO$ is a stable and reusable photocatalyst that may be suitable for the treatment of industrial effluent. The electrons in the VB of NiO, $SrCO_3$, and ZnO were stimulated and moved to the CB when NMs were exposed to visible light. At the same time, the same number of holes was created in VB. Through carrier diffusion among the NiO, $SrCO_3$, and ZnO, the electron is transferred from $SrCO_3$ (3.17 eV) to ZnO (3.2 eV) and finally to NiO (3.5 eV) at this point (electron transferred from lower energy CB to the higher energy CB during photoexcitation), and the hole transferred from NiO to ZnO and then to $SrCO_3$, until the system reached an equilibrium.[68,75,80] The electron and hole transfer processes were reversed during the emission of light. The multi-metal oxide system, creating heterojunctions with energy level perturbation, delayed the

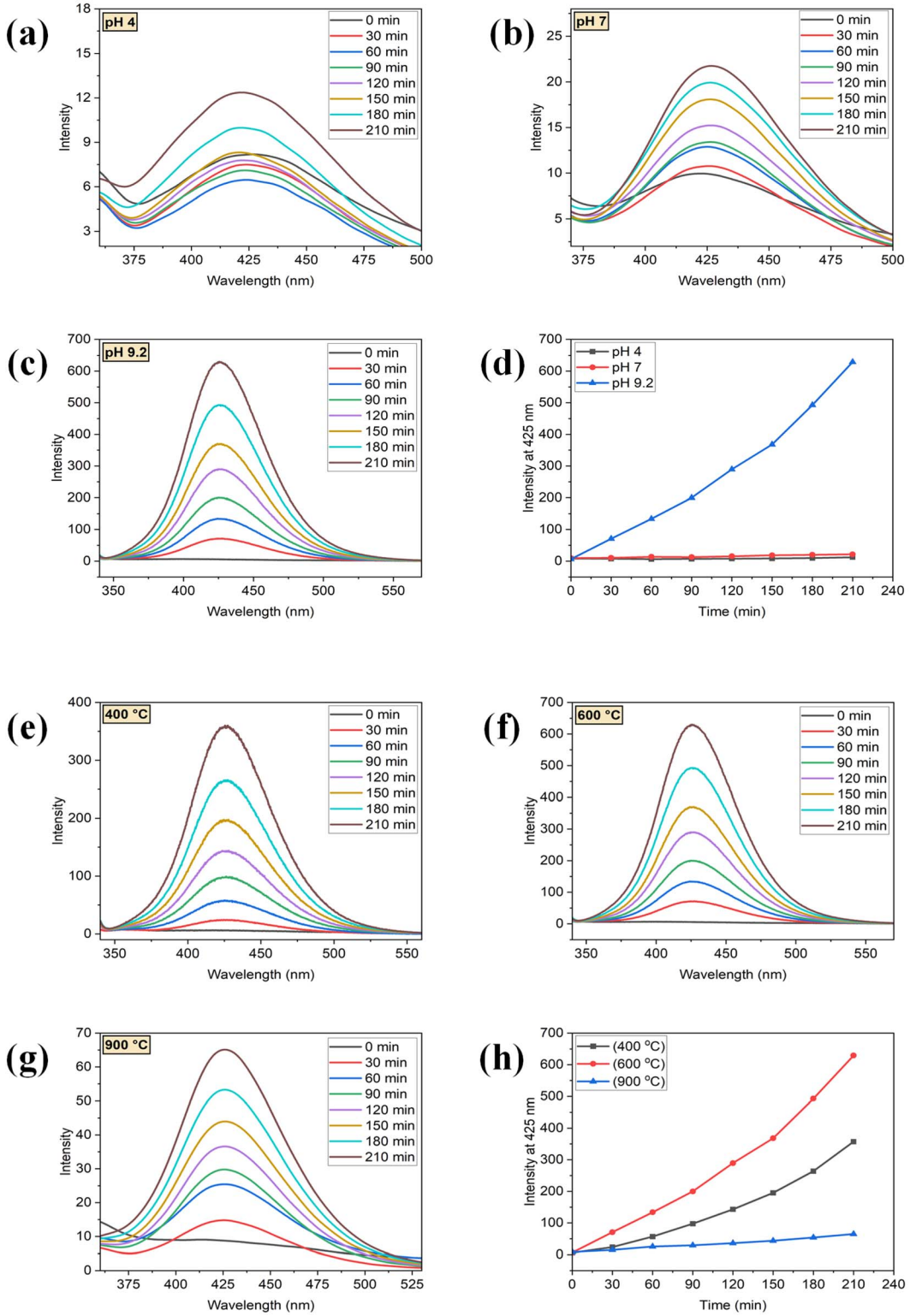

Fig. 4 Hydroxyl radical (˙OH) generation during photocatalysis of NiO·$SrCO_3$·ZnO NMs (a–d) at different pH and (e–h) with catalysts calcined at different temperatures (425 nm wavelength; under visible light).

electron–hole recombination process and accelerated the photocatalysis. The MB dye was degraded by the ROS (˙OH, $\cdot O_2^-$) produced during the energy transfer process. The non-fluorescent sodium terephthalate solution was used to identify the photocatalysis process of the ROS, the ˙OH radicals. Sodium terephthalate was converted into the fluorescently

active sodium 2-hydroxyterephthalate when it reacted with ˙OH radicals. The overall photocatalytic performance of $NiO \cdot SrCO_3 \cdot ZnO$ is illustrated in Fig. 5, which demonstrates how NMs break down the MB dye by producing ROS.

Antibacterial activity of $NiO \cdot SrCO_3 \cdot ZnO$ NMs

Extensive investigations into the potential of NMs as an antibacterial agent were conducted. The Agar Well Diffusion method was utilized to evaluate the antibacterial characteristics of the $NiO \cdot SrCO_3 \cdot ZnO$ NMs against a range of pathogenic bacteria, including Gram-positive (*S. aureus*) and Gram-negative (*K. pneumoniae*, *P. aeruginosa*, and *P. mirabilis*) bacteria. The pathogenic bacterial isolates were precultured at 37 °C at 120 rpm in nutrient-rich broth media. After that, they were held for around a day. Three different concentrations of NMs were used to create the samples: 1 mg mL^{-1}, 2 mg mL^{-1}, and 3 mg mL^{-1}. A well with a depth of roughly 6 mm was drilled into the

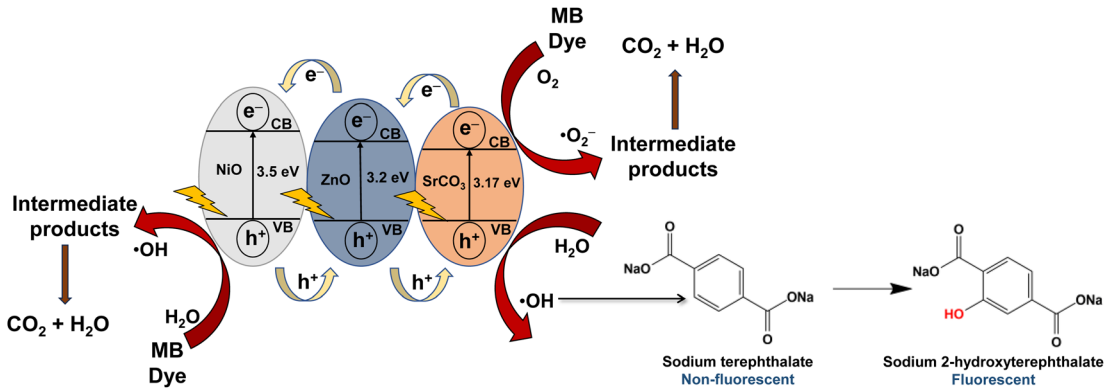

Fig. 5 A schematic of the energy levels of NiO, $SrCO_3$, and ZnO and photocatalytic degradation of MB dyes by the $NiO \cdot SrCO_3 \cdot ZnO$ NMs.

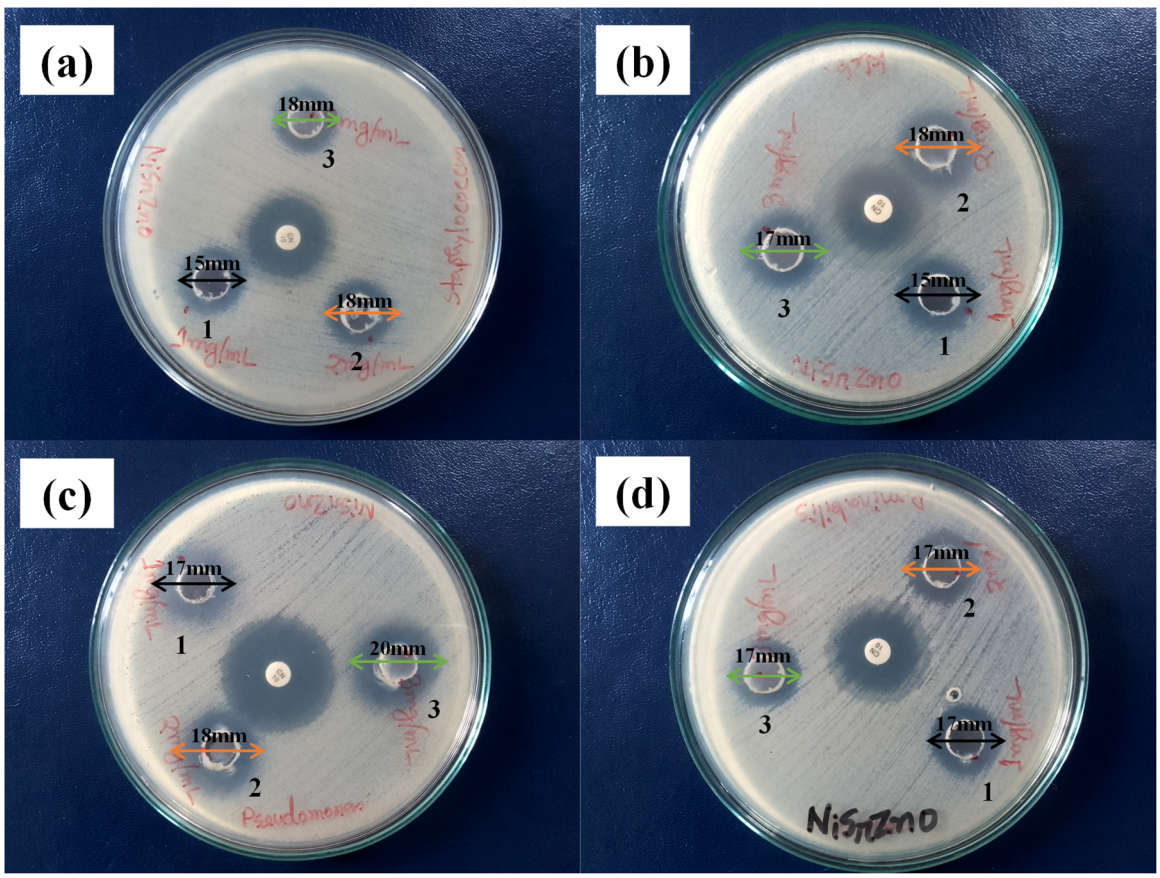

Fig. 6 Antibacterial activities of the $NiO \cdot SrCO_3 \cdot ZnO$ NMs with different concentrations of solutions, (1) 1 mg mL^{-1}, (2) 2 mg mL^{-1}, and (3) 3 mg mL^{-1}, in the presence of (a) *Staphylococcus aureus*, (b) *Klebsiella pneumonia*, (c) *Pseudomonas aeruginosa*, and (d) *Proteus mirabilis* (the central spot is for the control, CN 10).

agar material. 95 μL of the created NMs solutions were added to each well using a micropipette. As a control, gentamicin (CN 10) was used. The different levels of zone inhibition on the plates were assessed following about 24 hours of incubation at 37 °C. As seen in Fig. 6, the produced NMs demonstrated comparable bacterial killing power for both Gram-positive and Gram-

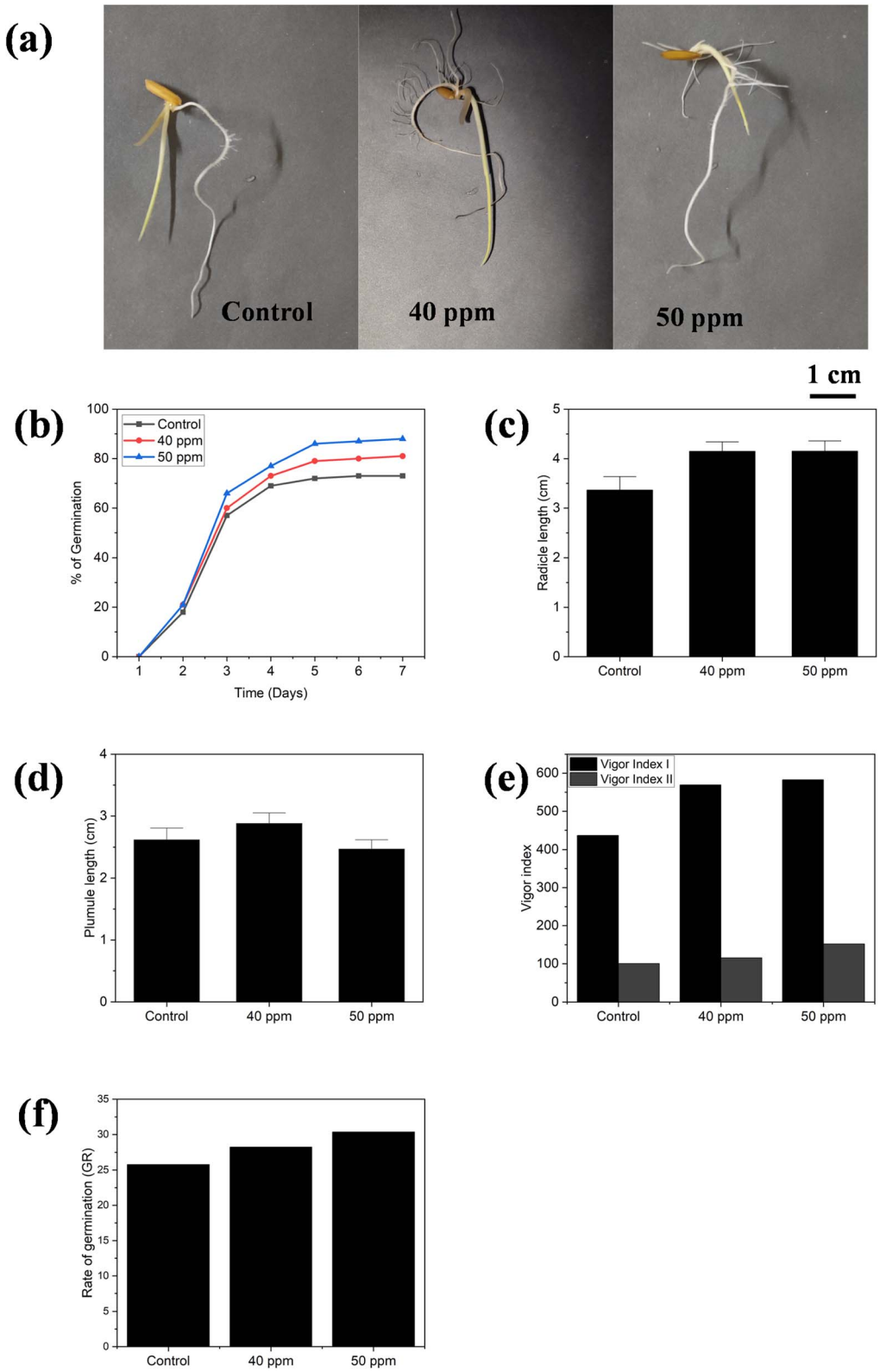

Fig. 7 Germination study of *Oryza sativa* by using $NiO{\cdot}SrCO_3{\cdot}ZnO$ NMs in a Petri dish (lab conditions). (a) Phenotype of rice seedlings after 7 days of germination, (b) germination percentage, (c) radicle length, (d) plumule length, (e) vigor index, and (f) rate of germination.

negative bacteria. As the concentration of NMs increased, the proliferation of *P. aeruginosa* reduced. Solution 3 had greater antibacterial efficacy than solutions 1 and 2. Table S5 presents the results of the investigation into the antibacterial characteristics of the produced NMs utilizing the Agar Well Diffusion method. Antibacterial activity is based on the reduced particle size of NMs and is regulated by different crystal morphologies and growth patterns.[81,82]

Germination assay for *Oryza sativa*

The seed germination assay for *Oryza sativa was performed* to evaluate the effect of nano-priming agents on seed germination. After 24 hours of imbibition, the seeds were taken and placed in a Petri dish to monitor the impact of the nano-priming agent on plant growth. Following seven days of observation, the germination outcome was recorded. The nano-primed rice seedlings exhibit phenotypic characteristics indicative of the absence of toxicity symptoms (Fig. 7(a)).

A germination study was performed using different concentrations of synthesized NMs of 30 to 70 ppm, with the 40 and 50 ppm samples exhibiting better germination and growth (Fig. S6). Further germination studies were executed by using these two concentrations of NMs. When compared to the control, priming rice seeds with 40 and 50 ppm NMs may increase the rate of germination percentage (%GP). After incubation, 21% of both the 40 and 50 ppm nano-primed seeds germinated on the second day, compared to 18% of the control seeds. Additionally, it was noticed that seeds treated with 40 and 50 ppm had achieved 60% and 66% germination, respectively, on the third day of incubation. On the seventh day, the % GP for the 40 and 50 ppm treatments was 81% and 88%, respectively. On the other hand, the control treatment %GP was 73%. According to reports, the %GP of seeds treated with 40 and 50 ppm was higher than that of the control (Fig. 7(b) and Table 1).

Nano-primed rice seedlings showed radicle and plumule length stimulation of almost 23% and 10%, respectively (Fig. 7(c and d)). Furthermore, the treated seedlings' rate of germination (GR) and germination vigor index were computed. Vigor index values showed a similar trend to %GP (Fig. 7(e)). It appears that NM treatment could enhance seed emergence and seedling establishment by raising the vigor index.[61] The GR values were observed to be gradually raised by the nano-priming treatment (Fig. 7(f)). %GP, vigor index, GR, and total seedling development were all enhanced by the nano-priming treatment at an ideal dosage of 50 ppm (Table 2). NMs are more effective because of their larger surface area and their enhanced adherence to the seed cell surface.[83]

After completing the germination study under lab conditions, the field-based germination was performed in sunlight. In field-based germination, soil was used (collected from cultivation land). Here, 10 seeds were treated with a control and 50 ppm of NMs. After 24 h of imbibition, the seeds were planted in a pot, and data were recorded after 10 days of germination. Out of 10 seeds, 7 and 9 seeds germinated in the control (Fig. 8(a)) and 50 ppm (Fig. 8(b)) nano-priming conditions, respectively. The root, shoot, and stem growth of 50 ppm NMs were more than 39%, 41% and 37% higher compared to the control, respectively (Fig. 8(c–e)). Also, the vigor index I observed was almost 50% higher (Fig. 8(f)). In the field-based germination experiment, 50 ppm NMs also had a positive impact.

Table 1 Germination percentage of *Oryza sativa* using the $NiO{\cdot}SrCO_3{\cdot}ZnO$ NMs in a Petri dish

	% of germination		
Time	Control	40 ppm	50 ppm
Day 1	0	0	0
Day 2	18	21	21
Day 3	57	60	66
Day 4	69	73	77
Day 5	72	79	86
Day 6	73	80	87
Day 7	73	81	88

Histochemical localization of ROS production during germination

According to Leymarie *et al.*,[84] ROS generation in germinating seeds should generally take place inside the oxidative window range necessary for ROS signalling. Any detachment from this range may result in germination inhibition. Thus, NBT staining was used to locate $^{\bullet}O_2^-$ in rice seeds that were germinating. The results showed that, compared to the control, NBT staining indicated a discernible increase in $^{\bullet}O_2^-$ in 40 and 50 ppm nano-priming seeds that germinated (Fig. 9). NBT stained the coleoptiles a light purple, suggesting that $^{\bullet}O_2^-$ could assist in cell elongation during germination, even though it caused purple stains in the radicle of 40 and 50 ppm nanoparticle treated seeds. Compared to the control, faster germination and greater seedling growth were made possible by an increase in antioxidant enzymes that regulated ROS production. ROS has a dual

Table 2 Parameters of *Oryza sativa* germination using $NiO{\cdot}SrCO_3{\cdot}ZnO$ NMs in a Petri dish (after 7 days of observation)

		Vigor index		
Treatment	% of germination (%GP)	Vigor index I	Vigor index II	Rate of germination (GR)
Control	73	436.59	100.37	25.77
40 ppm	81	569.39	115.62	28.26
50 ppm	88	582.76	151.86	30.36

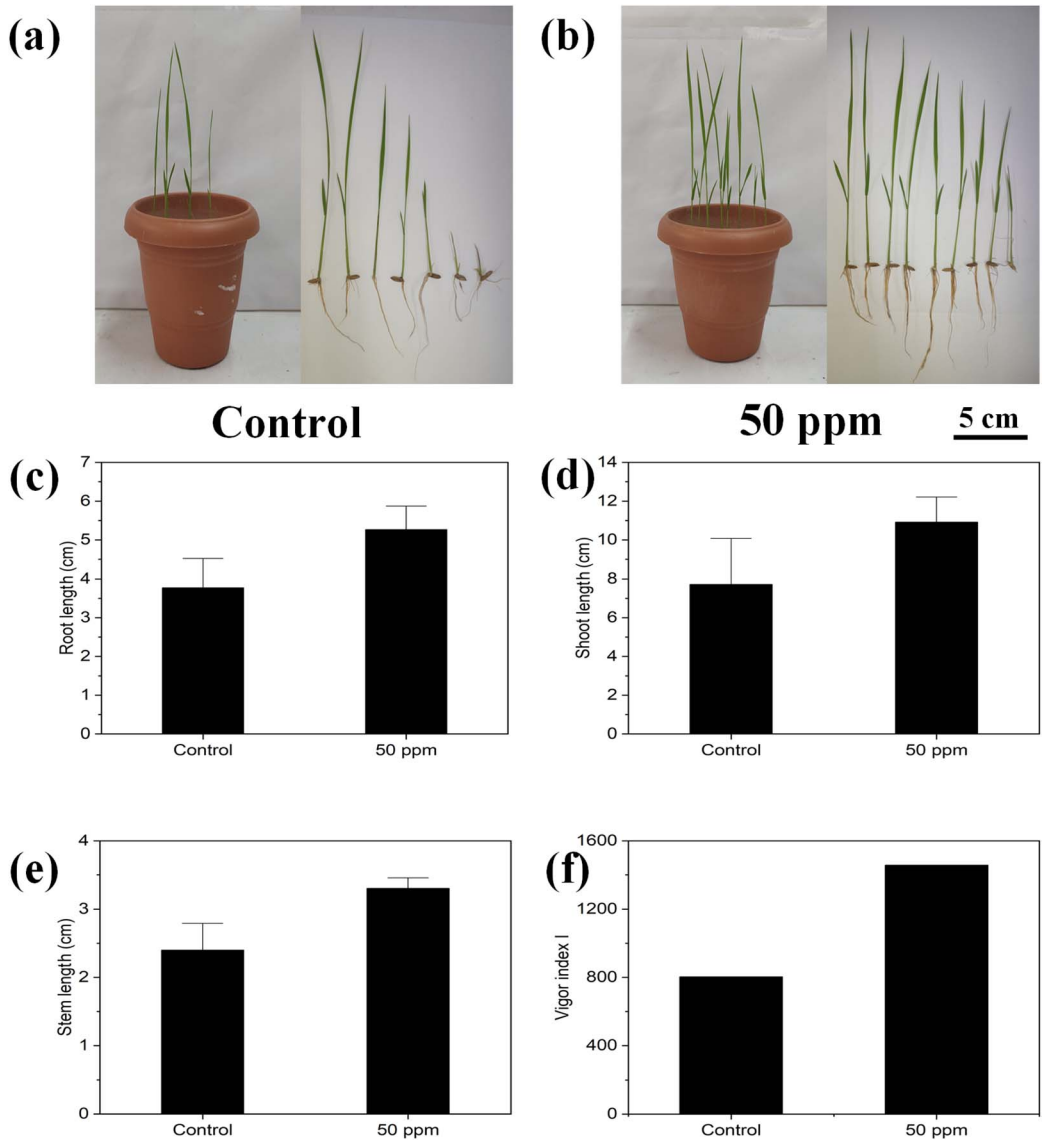

Fig. 8 Germination study of *Oryza sativa* by using the $NiO{\cdot}SrCO_3{\cdot}ZnO$ NMs in field-based experiments in sunlight, growth of seeds in (a) control and (b) 50 ppm NMs after 10 days of germination, (c) root length, (d) shoot length, (e) stem length, and (f) vigor index I.

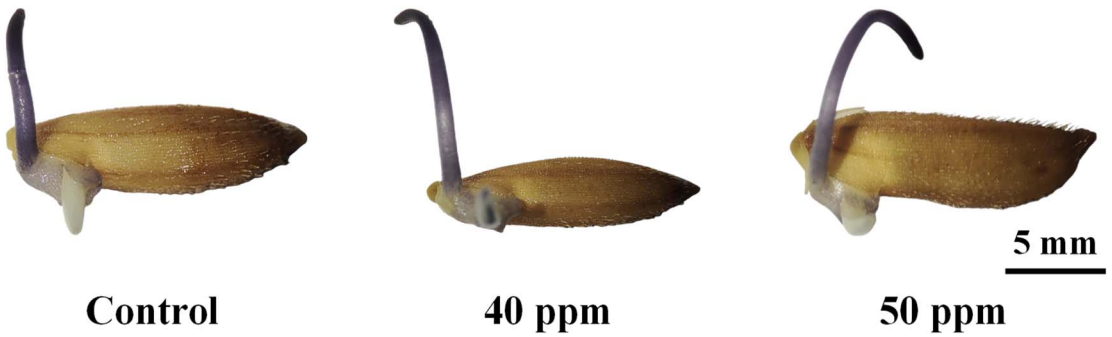

Fig. 9 Histochemical staining and quantification of the $^{\bullet}O_2^-$ content after 2 days of incubation of the *Oryza sativa* seeds in the respective conditions (control, 40 ppm, and 50 ppm).

role in seed germination, both contributing to oxidative stress and acting as a significant signaling molecule. Low ROS levels initially promote dormancy release and induce germination by influencing hormone levels and further cellular processes. However, excessive ROS levels can lead to seed deterioration. Thus, future studies on the determination of antioxidant enzymes involved in the seed germination process are expected to reveal more insights into seed germination and improve the utilization of nanoparticles as promoters of seed germination.[37]

Electrochemical characterization of $NiO \cdot SrCO_3 \cdot ZnO$ NMs as a chemical sensor

The urea sensor was fabricated utilizing a GCE covered with a thin coating of co-doped $NiO \cdot SrCO_3 \cdot ZnO$ nanomaterials. To augment the stability of this thin coating on the GCE, a few drops of Nafion (5% suspension in ethanol) were used as an adhesive, thereby enhancing its long-term performance. Nafion, as a conductive copolymer, improves the conductivity and electron transfer rate of the working electrode in the electrochemical sensor. Similar electrochemical phenomena have been described in our previous papers.[85–89] In the electrochemical detection of urea, currents were recorded at the surface of the co-doped $NiO \cdot SrCO_3 \cdot ZnO$ nanomaterials on the flat GCE. The holding duration at the Keithley electrometer was consistently set to 1 second for the studies. This approach is the first study utilizing co-doped $NiO \cdot SrCO_3 \cdot ZnO$ nanomaterials on glassy carbon electrodes as a urea sensor. During the electrochemical sensing process in a phosphate buffer solution, urea is oxidized on the $NiO \cdot SrCO_3 \cdot ZnO$ NMs/Nafion/GCE surface, producing N_2, CO_2, H_2O, and free electrons (Scheme 1). This oxidation increases the conductivity of the buffer medium, resulting in the observed *I–V* response. Similar urea oxidation processes have been studied in previous research.[90,91]

To comprehensively evaluate the $NiO \cdot SrCO_3 \cdot ZnO$ nanomaterials built on the GCE sensor, we performed an electrochemical investigation of several hazardous substances. The analyzed compounds comprised 1,2-diaminobenzene (1,2-DAB), 2,4-diaminophenol (2,4-DAP), 2,4-dinitrophenol (2,4-DNP), urea, 3-methoxyphenol (3-MP), 4-aminophenol (4-AP), 4-nitrophenyl hydrazine (4-NPHyd), benzaldehyde, and phenyl hydrazine (PHyd). Each chemical was evaluated at a concentration of 0.1 μM in a phosphate buffered solution at pH 7.0. As seen in Fig. 10(a), the electrochemical response indicated that urea generated the most pronounced *I–V* response among all evaluated chemicals. This finding indicates that urea can be effectively distinguished by the $NiO \cdot SrCO_3 \cdot ZnO$ NMs/Nafion/GCE sensor, making it the primary candidate for selective detection in this study. Recognizing the critical role of pH in electrochemical sensing, we further investigated the performance of the assembled sensor at various buffer pH levels to optimize urea detection. Fig. 10(b) illustrates that the $NiO \cdot SrCO_3 \cdot ZnO$ NMs/Nafion/GCE sensor attained the maximum oxidation current at pH 7.0. The appropriate pH

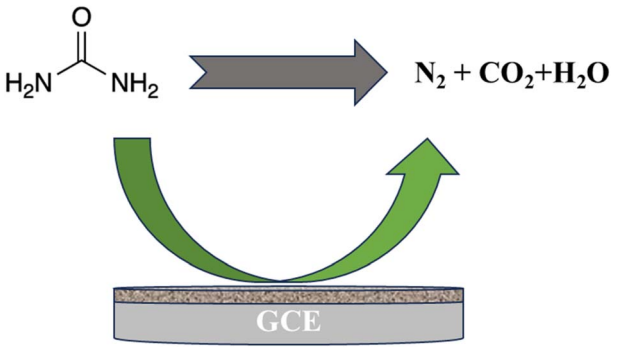

Scheme 1 The electrochemical detection of urea using the $NiO \cdot SrCO_3 \cdot ZnO$ NMs/Nafion/GCE electrode.

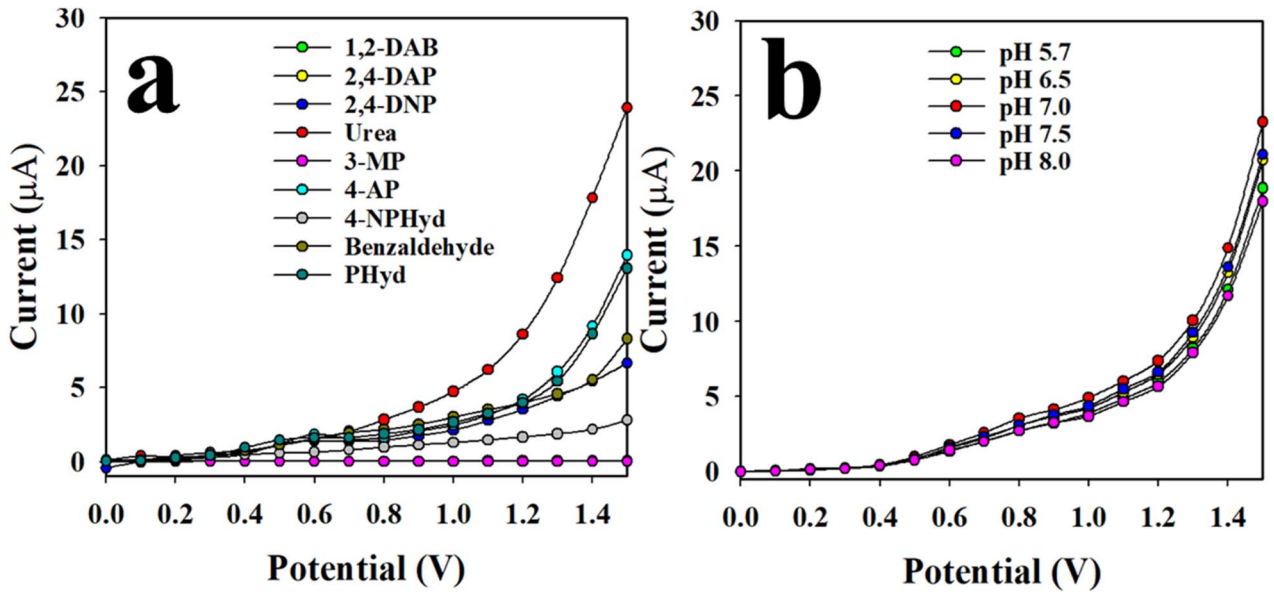

Fig. 10 Electrochemical characterization of the $NiO \cdot SrCO_3 \cdot ZnO$ NMs/Nafion/GCE sensor. (a) Selectivity and (b) pH effect in the detection of urea.

improves the sensor's sensitivity and selectivity for urea, validating its efficacy in detecting this hazardous chemical.

Having confirmed the sensor's selectivity for urea, we conducted *I–V* measurements on several urea solutions ranging from 0.1 nM to 0.1 mM, as shown in Fig. 11(a). The data demonstrated clear and different reactions for each concentration. Fig. 11(b) shows that the *I–V* responses exhibit a linear pattern, progressively rising from lower to higher urea concentrations. This trend indicates that the *I–V* responses vary proportionally with concentration, aligning with findings reported in our previous studies.[92–96] To establish a calibration curve for the proposed sensor, we plotted current against urea concentration, as shown in Fig. 11(b). The data presented were obtained at a potential of +1.5 V, as indicated by the results in Fig. 11(b). The sensitivity of the urea sensor was determined by dividing the slope of the calibration curve (0.7453 μA μM^{-1}) by the surface area of the glassy carbon electrode (0.0316 cm^2), resulting in a sensitivity of 23.5854 μA μM^{-1} cm^{-2}. Subsequently, we evaluated the linear dynamic range (LDR) by pinpointing the most linear segment of the calibration curve, which demonstrated a dynamic range of 0.1 nM to 0.01 mM, signifying a wide capacity for urea detection. Furthermore, we investigated the correlation between the logarithm of urea concentration and current, as shown in Fig. 11(c). The data fit resulted in a regression coefficient of $R^2 = 0.9910$, indicating a robust correlation that supports the linearity of the LDR. To determine the lower limit of urea detection, we applied a signal-to-noise (SNR) ratio of 3, which resulted in an impressive LOD of 4.31 ± 0.22 pM. This underscores the sensor's ability to effectively detect urea at extremely low concentrations.

To assess the study's dependability, many tests were performed, as shown in Fig. 12. The response time, defined as the interval required for a comprehensive *I–V* measurement of an analyte, is a vital indicator of the sensor's efficacy. The parameter was evaluated at a concentration of 0.1 μM urea in a buffer solution at pH 7.0, as shown in Fig. 12(a). The results indicate that the time–current graph stabilizes at about 25 seconds. Consequently, it can be inferred that the suggested urea sensor utilizing NiO·$SrCO_3$·ZnO NMs/Nafion/GCE necessitates 25

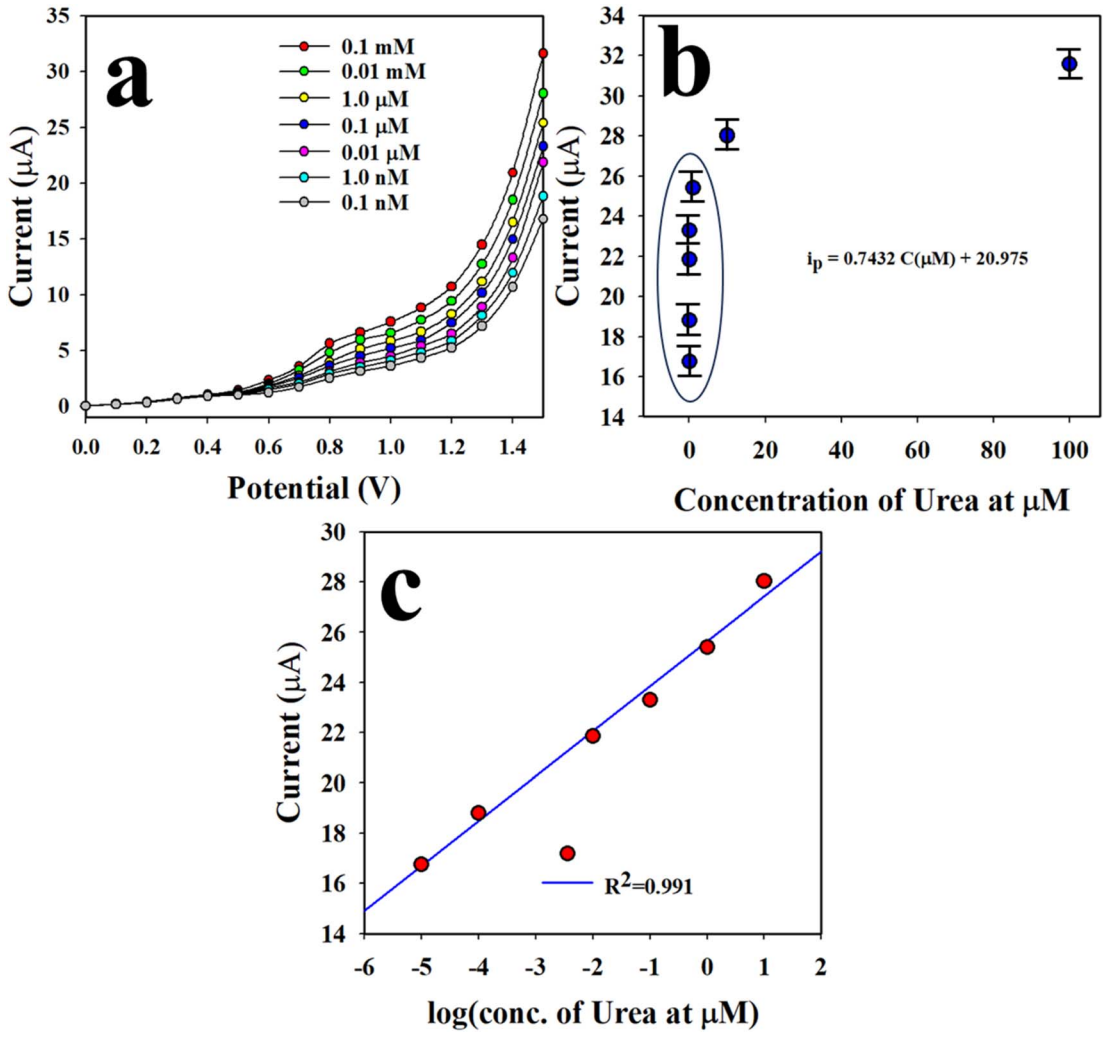

Fig. 11 (a) *I–V* responses of urea in the range of 0.1 nM to 0.1 mM in the buffer phase, (b) calibration of the urea sensor, and (c) log(concentration) *vs.* current plot.

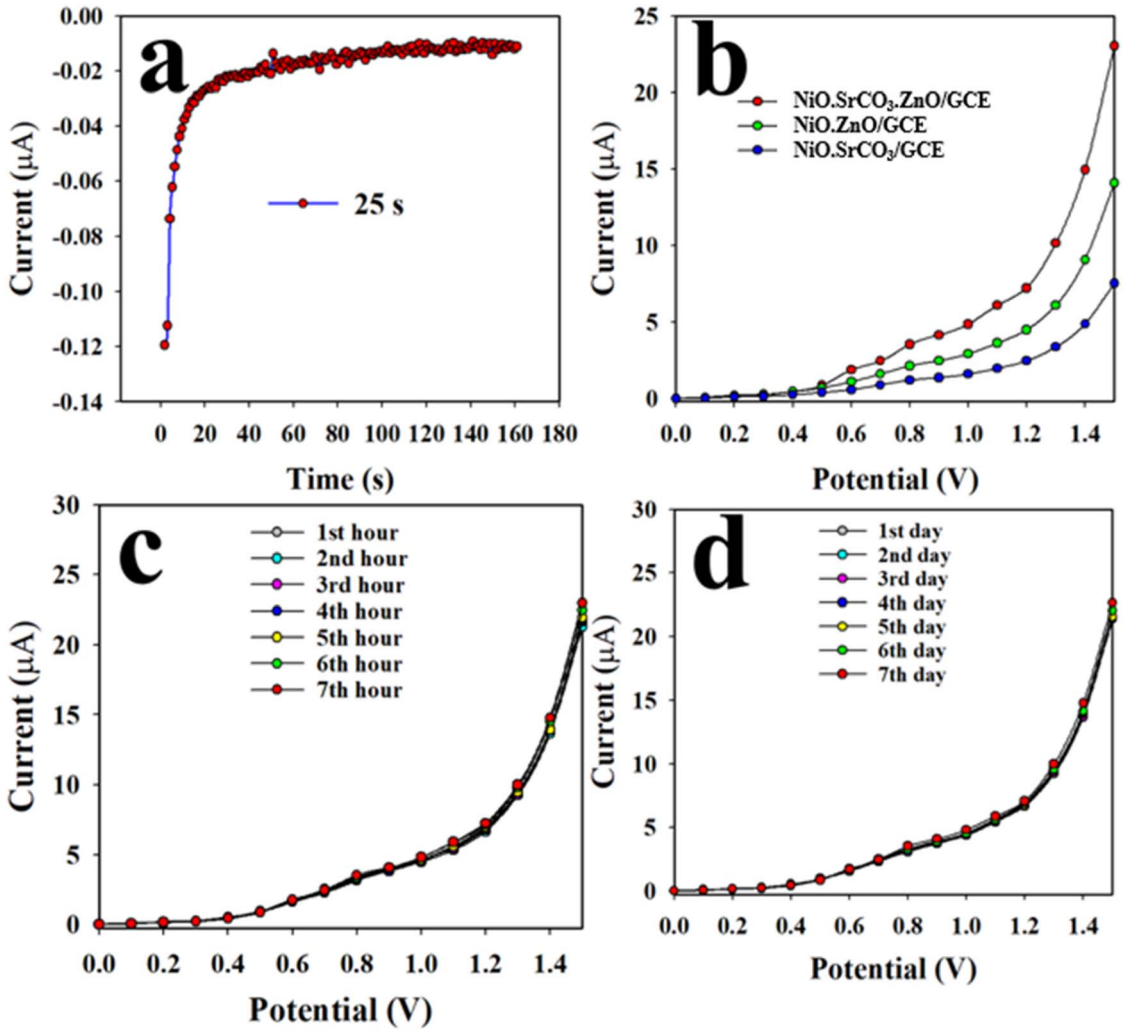

Fig. 12 (a) Examination of the response time of the urea sensor, (b) control experiments to validate the interference effect of the urea sensor in the presence of various electrolytes, (c) reproducibility assessment of the urea sensor, and (d) long-term performance evaluation of the urea sensor in the buffer phase.

seconds to finalize the *I–V* analysis of urea. This reaction time signifies a high level of efficiency for the sensor.

Fig. 12(b) shows the *I–V* oxidation of urea using various modified GCEs, including NiO·ZnO NPs/Nafion/GCE, $NiO \cdot SrCO_3$ NPs/Nafion/GCE, and $NiO \cdot SrCO_3 \cdot ZnO$ NMs/Nafion/GCE, in a pH 7.0 medium with a concentration of 0.1 μM urea. The data indicate that $NiO \cdot SrCO_3 \cdot ZnO$ NMs/Nafion/GCE produced the highest current at a potential of +1.5 V. This underscores the significance of employing ternary metal oxides in the development of urea sensors. Reproducibility serves as a critical metric for assessing the reliability of the urea sensor, reflecting the sensor's consistency. The statement pertains to the sensor's capacity to generate consistent *I–V* responses when subjected to the same conditions, including analyte concentration, buffer pH, and the range of applied potential. To evaluate this, experiments were performed at a concentration of 0.1 μM urea in a buffer solution with pH 7.0, as shown in Fig. 12(c). The outcomes of seven successive *I–V* analyses conducted over seven hours showed no significant variation, indicating that the proposed urea sensor is capable of consistently detecting unknown samples. The reproducibility was assessed through the relative standard deviation (RSD) at a potential of +1.5 V, resulting in an RSD of 1.45%, which signifies a high level of precision. Additionally, the long-term stability of the urea sensor during the buffer phase is essential for *I–V* analysis. The stability was assessed through the repetition of reproducibility tests conducted for seven days, as shown in Fig. 12(d), yielding consistent results.

To validate this study, it is important to compare the findings with those of similar research. Performance metrics are presented in Table 3,[97–102] focusing on sensitivity, LDR, and DL. Table 3 shows that the urea detection with the synthesized $NiO \cdot SrCO_3 \cdot ZnO$ NMs/Nafion/GCE offers enhanced parameters compared to those reported by previous authors.

Method validation with real samples

To determine the applicability of the urea sensor with $NiO \cdot SrCO_3 \cdot ZnO$ NMs/Nafion/GCE, various real samples underwent *I–V* analysis in the recovery method, with the results detailed

Table 3 Comparative study of urea detection based on various nanomaterials by using electrochemical approaches

Modified GCE	DL[a]	LDR[a]	Sensitivity[a]	Ref.
NiCu(OOH)/GCE	—	2.00–30.00 mM	10.72×10^{-3} μA μM^{-1} cm^{-2}	97
CuO/Co_3O_4/MWCNTs/SPE	0.223 pM	1.0–0.1 M	—	98
CuO/c-MWCNT/GCE	0.16 mM	2–8 mM	—	99
$NiCo_2O_4$/3DG NCs/ITO	5.0 μM	0.06–0.30 mM	0.166 μA μM^{-1} cm^{-2}	100
Ag–N-SWCNTs/GCE	4.7 nM	66–20.6 mM	0.141 μA μM^{-1} cm^{-2}	101
$NiCo_2O_4$ NNs/GCE	1.0 μM	0.01–5 mM	—	102
$NiO \cdot SrCO_3 \cdot ZnO$ NMs/Nafion/GCE	4.31 pM	0.1–0.01 mM	23.58 μA μM^{-1} cm^{-2}	This study

[a] DL (detection limit), LDR (linear dynamic range), pM (picomole), mM (millimole).

Table 4 Testing of biological samples using the $NiO \cdot SrCO_3 \cdot ZnO$ NMs/Nafion/GCE sensor with the recovery system

Sample	Added urea concentration (μM)	Measured urea conc.[a] by $NiO \cdot SrCO_3 \cdot ZnO$ NMs/Nafion/GCE (μM)			Average recovery[b] (%)	RSD[c] (%) ($n = 3$)
		R1	R2	R3		
Human serum	0.0100	0.0098	0.0101	0.0097	98.7	2.11
Mouse serum	0.0100	0.0102	0.0097	0.0101	103.0	2.65
Rabbit serum	0.0100	0.0101	0.0104	0.0098	101.0	2.97

[a] Mean of three repeated determinations (signal to noise ratio of 3) $NiO \cdot SrCO_3 \cdot ZnO$ NMs/GCE. [b] Concentration of urea determined/conc taken (unit: μM). [c] Relative standard deviation value indicates precision of three repeated measurements (R1, R2, and R3).

in Table 4. The evaluation of human, mouse, and rabbit serum indicates satisfactory results.

Conclusion

In summary, the synthesis of $NiO \cdot SrCO_3 \cdot ZnO$ NMs was accomplished using a low-cost, simple, and easily controllable co-precipitation approach. The NMs were characterized by using XRD, SEM, EDS, FTIR, Raman, and PL analyses. The NMs were examined for their photocatalytic activity using various factors, including contact time, pH influence, temperature effect, reusability of the catalysts, and catalytic doses. At pH 9.2, the highest photocatalytic efficiency (98.41%) was observed with 0.06 g per L NMs. The NMs exhibited good photocatalytic activity at pH 9.2 rather than pH 7 and 4. Moreover, NMs calcined at 600 °C exhibited better photocatalytic activity than those calcined at 400 °C and 900 °C. The reusability of the synthesized NMs was excellent, with an efficiency loss of 0.62% for the 4th time of reuse for $NiO \cdot SrCO_3 \cdot ZnO$. Hydroxyl radicals ($^{\bullet}OH$) were detected during photocatalysis, which were responsible for dye degradation. The generation of the $^{\bullet}OH$ radical increased with time, dependent on visible light irradiation. The generation of radicals was higher in the basic medium for NMs calcined at 600 °C, which supports the photocatalytic activity. The NMs also exhibited excellent bacterial killing activity against both Gram-positive and Gram-negative bacteria. The germination study on *Oryza sativa by using* $NiO \cdot SrCO_3 \cdot ZnO$ NMs showed positive results and influenced the seed growth in both laboratory and field experiments. In the Petri dish experiments (lab experiments), the growth of seeds was higher in the treated seeds compared with the control. The same result was observed in the field-based experiments. In the field-based experiment, all parameters (germination, vigor index, stem, root, and shoot length) were higher for the nano-priming seeds, which indicated that the NM-treated seeds show positive results in sunlight. Also, the $^{\bullet}O_2^-$ radical detection supported the positive impact of NMs in rice seed germination.

The developed co-doped $NiO \cdot SrCO_3 \cdot ZnO$ nanomaterials were systematically layered onto GCE using 5% Nafion adhesive to create the urea sensor. The sensor demonstrated notable performance metrics, featuring sensitivity (23.5854 μA μM^{-1} cm^{-2}), LDR (0.1 nM to 0.01 mM), and a DL of 4.31 ± 0.22 pM. Additionally, it demonstrated excellent reproducibility, response time, resistance to interference, and long-term performance. The analysis of several real samples further confirmed its reliability and validity.

Conflicts of interest

There are no conflicts to declare.

Data availability

Data will be available upon a reasonable request from the corresponding author. Supplementary information is available. See DOI: https://doi.org/10.1039/d5ra06318c.

Acknowledgements

The author acknowledged the SUST Research Grant (No. PS/2022/1/09) for support. This Project was funded by the Deanship of Scientific Research (DSR) at King Abdulaziz University, Jeddah, Saudi Arabia, under grant no. (IPP: 186-961-2025). The authors, therefore, acknowledge with thanks DSR for technical

and financial support. Md Abdus Subhan acknowledged SUST for a sabbatical leave and his current affiliation, Texas Tech University, Lubbock, TX, USA, for support.

References

1 L. Sun, X. Hong, P. Zou, X. Chu and Y. Liu, *J. Alloys Compd.*, 2012, **535**, 91–94.
2 X. Wang, J. C. Hanson, G. Liu, J. A. Rodriguez, A. Iglesias-Juez and M. Fernández-García, *J. Chem. Phys.*, 2004, **121**(11), 5434–5444.
3 W. Lu, D. Sun and H. Yu, *J. Alloys Compd.*, 2013, **546**, 229–233.
4 M. A. Subhan, S. A. Monim, M. B. R. Bhuiyan, A. N. Chowdhury, M. Islam and M. A. Hoque, *Open J. Inorg. Chem.*, 2011, **1**(2), 9.
5 J. J. S. Teles, E. R. Faria, J. H. M. Santos, L. G. D. Sousa, D. V. Franco, W. G. Nunes, H. Zanin and L. M. D. Silva, *Electrochim. Acta*, 2019, **295**, 302–315.
6 M. B. Gawande, R. K. Pandey and R. V. Jayaram, *Catal. Sci. Technol.*, 2012, **2**(6), 1113–1125.
7 M. Pavan, S. Rühle, A. Ginsburg, D. A. Keller, H. N. Barad, P. M. Sberna, D. Nunes, R. Martins, A. Y. Anderson, A. Zaban and E. Fortunato, *Sol. Energy Mater. Sol. Cells*, 2015, **132**, 549–556.
8 M. Asamoto, S. Miyake, K. Sugihara and H. Yahiro, *Electrochem. Commun.*, 2009, **11**(7), 1508–1511.
9 M. S. Park, G. X. Wang, Y. M. Kang, D. Wexler, S. X. Dou and H. K. Liu, *Angew. Chem., Int. Ed.*, 2007, **46**(5), 750.
10 J. L. Barrio-Manso, P. Calvo, F. C. García, J. L. Pablos, T. Torroba and J. M. García, *Polym. Chem.*, 2013, **4**(15), 4256–4264.
11 F. Ahmadi Tabar, A. Nikfarjam, N. Tavakoli, J. Nasrollah Gavgani, M. Mahyari and S. G. Hosseini, *Microchim. Acta*, 2020, **187**, 293.
12 P. Pathak, S. Park and H. J. Cho, *Micromachines*, 2020, **11**(4), 368.
13 J. W. Rasmussen, E. Martinez, P. Louka and D. G. Wingett, *Expert Opin. Drug Delivery*, 2010, **7**(9), 1063–1077.
14 M. P. Vinardell and M. Mitjans, *Nanooncology Eng. Nanomater. Cancer Ther. Diagnosis*, 2018, pp. 341–364.
15 Y. Li, W. Zhang, J. Niu and Y. Chen, *ACS Nano*, 2012, **6**(6), 5164–5173.
16 A. C. Janaki, E. Sailatha and S. Gunasekaran, *Spectrochim. Acta, Part A*, 2015, **144**, 17–22.
17 Y. Liu, R. Njuguna, T. Matthews, W. J. Akers, G. P. Sudlow, S. B. Mondal, R. Tang, V. Gruev and S. Achilefu, *J. Biomed. Opt.*, 2013, **18**(10), 101303.
18 M. K. Debanath and S. Karmakar, *Mater. Lett.*, 2013, **111**, 116–119.
19 M. Shi, T. Qiu, B. Tang, G. Zhang, R. Yao, W. Xu, J. Chen, X. Fu, H. Ning and J. Peng, *Micromachines*, 2021, **12**(1), 80.
20 G. T. Anand, R. Nithiyavathi, R. Ramesh, S. J. Sundaram and K. Kaviyarasu, *Surf. Interfaces*, 2020, **18**, 100460.
21 A. Akbari, Z. Sabouri, H. A. Hosseini, A. Hashemzadeh, M. Khatami and M. Darroudi, *Inorg. Chem. Commun.*, 2020, **115**, 107867.
22 M. K. Aziz, S. Chauhan, Z. Azim, G. K. Bharati and S. Srivastava, *Int. J. Sci. Res. Arch.*, 2022, **7**(2), 245–254.
23 S. Uddin, L. B. Safdar, J. Iqbal, T. Yaseen, S. Laila, S. Anwar, B. A. Abbasi, M. S. Saif and U. M. Quraishi, *Microsc. Res. Tech.*, 2021, **84**(9), 2004–2016.
24 L. Song, S. Zhang and B. Chen, *Catal. Commun.*, 2009, **10**(12), 1565–1568.
25 A. Divya, T. Mathavan, S. Harish, J. Archana, A. M. F. Benial, Y. Hayakawa and M. Navaneethan, *Appl. Surf. Sci.*, 2019, **487**, 1271–1278.
26 W. Y. Qian, D. M. Sun, R. R. Zhu, X. L. Du, H. Liu and S. L. Wang, *Int. J. Nanomed.*, 2012, **7**, 5781–5792.
27 F. Wu, Q. Fang, S. Yan, L. Pan, X. Tang and W. Ye, *Environ. Sci. Pollut. Res.*, 2020, **27**, 26974–26981.
28 A. Singh, R. S. Sengar, V. D. Rajput, S. Agrawal, K. Ghazaryan, T. Minkina, A. R. M. Al Tawaha, O. M. Al Zoubi and T. Habeeb, *J. Ecol. Eng.*, 2023, **24**(10), 142–156.
29 D. Wang, L. Zhao, H. Ma, H. Zhang and L. H. Guo, *Environ. Sci. Technol.*, 2017, **51**(17), 10137–10145.
30 S. Verma and R. K. Dutta, *J. Environ. Chem. Eng.*, 2017, **5**(5), 4776–4787.
31 I. Y. Habib, J. Burhan, F. Jaladi, C. M. Lim, A. Usman, N. T. R. N. Kumara, S. C. E. Tsang and A. H. Mahadi, *Catal. Today*, 2021, **375**, 506–513.
32 E. Asenath-Smith, E. K. Ambrogi, E. Barnes and J. A. Brame, *Colloids Surf., A*, 2020, **603**, 125179.
33 H. A. Foster, I. B. Ditta, S. Varghese and A. Steele, *Appl. Microbiol. Biotechnol.*, 2011, **90**, 1847–1868.
34 R. K. Dutta, B. P. Nenavathu, M. K. Gangishetty and A. V. R. Reddy, *Colloids Surf., B*, 2012, **94**, 143–150.
35 G. Sharma, D. Prema, K. S. Venkataprasanna, J. Prakash, S. Sahabuddin and G. D. Venkatasubbu, *Arabian J. Chem.*, 2020, **13**(11), 7680–7694.
36 M. A. Farooq, X. Zhang, M. M. Zafar, W. Ma and J. Zhao, *Front. Plant Sci.*, 2021, **12**, 781734.
37 S. Afzal, D. Sharma and N. K. Singh, *Environ. Sci. Pollut. Res.*, 2021, **28**, 40275–40287.
38 S. Swify, R. Mažeika, J. Baltrusaitis, D. Drapanauskaitė and K. Barčauskaitė, *Sustainability*, 2023, **16**(1), 188.
39 A. M. Motasim, A. W. Samsuri, A. Nabayi, A. Akter, M. A. Haque, A. S. Abdul Sukor and A. M. Adibah, *Discov. Agric.*, 2024, **2**(1), 42.
40 R. Vanholder, T. Gryp and G. Glorieux, *Nephrol., Dial., Transplant.*, 2018, **33**(1), 4–12.
41 H. Wang, H. Zhang, D. Zhang, J. Wang, H. Tan and T. Kong, *J. Cleaner Prod.*, 2021, **315**, 128149.
42 C. K. Choi, S. M. Shaban, B. S. Moon, D. G. Pyun and D. H. Kim, *Anal. Chim. Acta*, 2021, **1170**, 338630.
43 K. Berketa, O. Saiapina, L. Fayura, A. Sibirny, S. Dzyadevych and O. Soldatkin, *Sens. Actuators, B*, 2022, **367**, 132023.
44 T. Sakurai, T. Irii and K. Iwadate, *Leg. Med.*, 2022, **55**, 102011.
45 B. Doğan, A. Elik and N. Altunay, *Microchem. J.*, 2020, **154**, 104645.
46 M. Qafary, K. Khajeh, M. Ramazzotti, A. A. Moosavi-Movahedi and F. Chiti, *Int. J. Biol. Macromol.*, 2021, **174**, 32–41.

47 N. Ezzat, M. A. Hefnawy, S. A. Fadlallah, R. M. El-Sherif and S. S. Medany, *Sci. Rep.*, 2024, **14**(1), 14818.
48 T. S. K. Naik, S. Singh, P. Narasimhappa, R. Varshney, J. Singh, N. A. Khan, S. Zahmatkesh, P. C. Ramamurthy, N. Shehata, G. N. Kiran and K. Sunil, *Sci. Rep.*, 2023, **13**(1), 19995.
49 R. Paulose, R. Mohan and V. Parihar, *Nano-Struct. Nano-Objects*, 2017, **11**, 102–111.
50 Z. Wang, G. He, H. Yin, W. Bai and D. Ding, *Appl. Surf. Sci.*, 2017, **411**, 197–204.
51 V. Parihar, M. Raja and R. Paulose, *Rev. Adv. Mater. Sci.*, 2018, **53**(2), 119–130.
52 A. S. Danial, M. M. Saleh, S. A. Salih and M. I. Awad, *J. Power Sources*, 2015, **293**, 101–108.
53 J. Jin, S. Chen, J. Wang, C. Chen and T. Peng, *Appl. Surf. Sci.*, 2019, **476**, 937–947.
54 S. Yu, H. Wang, C. Hu, Q. Zhu, N. Qiao and B. Xu, *J. Mater. Chem. A*, 2016, **4**(42), 16341–16348.
55 Y. T. Chang, J. Y. Chen, T. P. Yang, C. W. Huang, C. H. Chiu, P. H. Yeh and W. W. Wu, *Nano Energy*, 2014, **8**, 291–296.
56 P. Ptáček, E. Bartoníčková, J. Švec, T. Opravil, F. Šoukal and F. Frajkorová, *Ceram. Int.*, 2015, **41**(1), 115–126.
57 L. Ye, J. Liu, Z. Jiang, T. Peng and L. Zan, *Appl. Catal., B*, 2013, **142**, 1–7.
58 K. A. Sultana, M. T. Islam, J. A. Silva, R. S. Turley, J. A. Hernandez-Viezcas, J. L. Gardea-Torresdey and J. C. Noveron, *J. Mol. Liq.*, 2020, **307**, 112931.
59 A. Vashisth and S. Nagarajan, *J. Plant Physiol.*, 2010, **167**(2), 149–156.
60 C. S. Vibhuti, K. Bargali and S. S. Bargali, *Indian J. Agric. Sci.*, 2015, **85**(1), 102–108.
61 H. Feizi, M. Kamali, L. Jafari and P. Rezvani Moghaddam, *Chemosphere*, 2013, **91**(4), 506–511.
62 W. Mahakham, A. K. Sarmah, S. Maensiri and P. Theerakulpisut, *Sci. Rep.*, 2017, **7**(1), 8263.
63 Q. Huang, C. Wang and Q. Shan, *Nanomaterials*, 2022, **12**(14), 2320.
64 M. El-Kemary, N. Nagy and I. El-Mehasseb, *Mater. Sci. Semicond. Process.*, 2013, **16**(6), 1747–1752.
65 M. H. Koupaei, B. Shareghi, A. A. Saboury, F. Davar, A. Semnani and M. Evini, *RSC Adv.*, 2016, **6**(48), 42313–42323.
66 T. Thongtem, N. Tipcompor, A. Phuruangrat and S. Thongtem, *Mater. Lett.*, 2010, **64**(4), 510–512.
67 V. M. Shajudheen, M. Sivakumar and S. S. Kumar, *Mater. Today: Proc.*, 2016, **3**(6), 2450–2456.
68 S. Ni, X. Yang and T. Li, *Mater. Lett.*, 2011, **65**(4), 766–768.
69 R. Cuscó, E. Alarcón-Lladó, J. Ibáñez, L. Artús, J. Jiménez, B. Wang and M. J. Callahan, *Phys. Rev. B: Condens. Matter Mater. Phys.*, 2007, **75**(16), 165202.
70 N. Al-Zaqri, K. Umamakeshvari, V. Mohana, A. Muthuvel and A. Boshaala, *J. Mater. Sci.: Mater. Electron.*, 2022, **33**(15), 11864–11880.
71 A. Rasool, M. C. Santhosh Kumar, M. H. Mamat, C. Gopalakrishnan and R. Amiruddin, *J. Mater. Sci.: Mater. Electron.*, 2020, **31**(9), 7100–7113.
72 A. Negash, S. Mohammed, H. D. Weldekirstos, A. D. Ambaye and M. Gashu, *Sci. Rep.*, 2023, **13**(1), 22234.
73 V. Singh, R. Sapehia and V. Dhiman, *Inorg. Chem. Commun.*, 2024, **162**, 112267.
74 G. E. Hernández-Villegas, W. J. Pech-Rodríguez, G. G. Suarez-Velázquez and C. A. Calles-Arriaga, *Emergent Mater.*, 2025, 1–15.
75 C. Luo, D. Li, W. Wu, Y. Zhang and C. Pan, *RSC Adv.*, 2014, **4**(6), 3090–3095.
76 M. A. Subhan, T. P. Rifat, P. C. Saha, M. M. Alam, A. M. Asiri, T. Raihan, A. K. Azad, W. Ghann, J. Uddin and M. M. Rahman, *New J. Chem.*, 2021, **45**(3), 1634–1650.
77 S. Bano, N. Ahmad, S. Sultana, S. Sabir and M. Z. Khan, *J. Environ. Chem. Eng.*, 2019, **7**(2), 103012.
78 L. Wang, J. Ge, A. Wang, M. Deng, X. Wang, S. Bai, R. Li, J. Jiang, Q. Zhang, Y. Luo and Y. Xiong, *Angew. Chem., Int. Ed.*, 2014, **53**(20), 5107–5111.
79 M. M. H. Masum, M. B. Islam, M. R. Anowar, K. Arsh and S. Alam, *Discov. Environ.*, 2025, **3**(1), 59.
80 J. Wu, C. Luo, D. Li, Q. Fu and C. Pan, *J. Mater. Sci.*, 2017, **52**(3), 1285–1295.
81 C. Buzea, I. I. Pacheco and K. Robbie, *Biointerphases*, 2007, **2**(4), MR17–MR71.
82 K. H. Adibkia, M. Barzegar-Jalali, A. Nokhodchi, M. R. Siahi Shadbad, Y. A. Omidi, Y. Javadzadeh and G. H. Mohammadi, *Pharm. Sci.*, 2009, **15**(4), 303–314.
83 V. Shah and I. Belozerova, *Water, Air, Soil Pollut.*, 2009, **197**, 143–148.
84 J. Leymarie, G. Vitkauskaité, H. H. Hoang, E. Gendreau, V. Chazoule, P. Meimoun, F. Corbineau, H. El-Maarouf-Bouteau and C. Bailly, *Plant Cell Physiol.*, 2012, **53**(1), 96–106.
85 M. M. Rahman, M. M. Alam and A. M. Asiri, *RSC Adv.*, 2018, **8**(2), 960–970.
86 M. M. Rahman, M. M. Alam and A. M. Asiri, *New J. Chem.*, 2018, **42**(12), 10263–10270.
87 M. M. Rahman, M. M. Alam, A. M. Asiri and M. A. Islam, *RSC Adv.*, 2017, **7**(37), 22627–22639.
88 M. M. Rahman, M. M. Alam, A. M. Asiri and M. R. Awual, *New J. Chem.*, 2017, **41**(17), 9159–9169.
89 M. M. Rahman, M. M. Alam and A. M. Asiri, *New J. Chem.*, 2017, **41**(18), 9938–9946.
90 V. Sanko, A. Şenocak, S. O. Tümay and E. Demirbas, *Bioelectrochemistry*, 2023, **149**, 108324.
91 G. Dhawan, G. Sumana and B. D. Malhotra, *Biochem. Eng. J.*, 2009, **44**(1), 42–52.
92 M. M. Rahman, M. M. Alam and A. M. Asiri, *J. Ind. Eng. Chem.*, 2018, **62**, 392–400.
93 M. M. Alam, A. M. Asiri, M. T. Uddin, M. A. Islam and M. M. Rahman, *RSC Adv.*, 2018, **8**(23), 12562–12572.

94 M. A. Subhan, P. C. Saha, M. M. Alam, A. M. Asiri, M. Al-Mamun and M. M. Rahman, *J. Environ. Chem. Eng.*, 2018, **6**(1), 1396–1403.
95 M. M. Rahman, M. M. Alam, A. M. Asiri and M. A. Islam, *Talanta*, 2018, **176**, 17–25.
96 M. M. Rahman, M. M. Alam, A. M. Asiri and M. A. Islam, *Talanta*, 2017, **170**, 215–223.
97 J. Yoon, M. Sim, T. S. Oh, Y. S. Yoon and D. J. Kim, *J. Electrochem. Soc.*, 2021, **168**(11), 117510.
98 H. S. Magar, R. Y. A. Hassan and M. N. Abbas, *Sci. Rep.*, 2023, **13**(1), 2034.
99 G. Padmalaya, B. S. Rathi, P. S. Kumar and G. Rangasamy, *Desalin. Water Treat.*, 2024, **320**, 100701.
100 N. S. Nguyen, G. Das and H. H. Yoon, *Biosens. Bioelectron.*, 2016, **77**, 372–377.
101 T. H. V. Kumar and A. K. Sundramoorthy, *J. Electrochem. Soc.*, 2018, **165**(8), B3006.
102 S. Amin, A. Tahira, A. Solangi, V. Beni, J. R. Morante, X. Liu, M. Falhman, R. Mazzaro, Z. H. Ibupoto and A. Vomiero, *RSC Adv.*, 2019, **9**(25), 14443–14451.